Pontifícia Universidade Católica
do Rio de Janeiro

João Pedro Torres de Sousa Andrade

Development and assessment of a simplified automatic impedance matching network for electromagnetic acoustic transducers.

Dissertação de Mestrado

Thesis presented to the Programa de Pós–Graduação em Engenharia Elétricada PUC-Rio in partial fulfillment of the requirements for the degree of Mestre em Engenharia Elétrica.

Advisor : Prof. Alan Conci Kubrusly
Co-advisor: Dr. Vivian Suzano Medeiros

Rio de Janeiro
June 2023

Pontifícia Universidade Católica do Rio de Janeiro

João Pedro Torres de Sousa Andrade

Development and assessment of a simplified automatic impedance matching network for electromagnetic acoustic transducers.

Thesis presented to the Programa de Pós–Graduação em Engenharia Elétricada PUC-Rio in partial fulfillment of the requirements for the degree of Mestre em Engenharia Elétrica. Approved by the undersigned Examination Committee.

Prof. Alan Conci Kubrusly
Advisor
Centro de Estudos em Telecomunicações – PUC-Rio

Dr. Vivian Suzano Medeiros
Co-advisor
CCPE – PUC-Rio

Dr. Marcelo Roberto Jimenez
Centro de Estudos em Telecomunicações – PUC-Rio

Prof. Eduardo Costa da Silva
Deparamento de Engenharia Elétrica – PUC-Rio

Rio de Janeiro, June the 31st, 2023

João Pedro Torres de Sousa Andrade

Graduated in Control and Automation Engineering from the Pontifical Catholic University of Rio de Janeiro - PUC-Rio - in 2021.

Bibliographic data

Torres de Sousa Andrade, João Pedro

Development and assessment of a simplified automatic impedance matching network for electromagnetic acoustic transducers. / João Pedro Torres de Sousa Andrade; advisor: Alan Conci Kubrusly; co-advisor: Vivian Suzano Medeiros. – Rio de Janeiro: PUC-Rio, Departamento de Engenharia Elétrica, 2023.

v., 68 f: il. color. ; 30 cm

Dissertação (mestrado) - Pontifícia Universidade Católica do Rio de Janeiro, Departamento de Engenharia Elétrica.

Inclui bibliografia

1. Engenharia Elétrica – Teses. 2. Eletromagnetismo Aplicado – Teses. 3. Transdutores Acústicos Eletromagnéticos;. 4. Ensaios Não destrutivos;. 5. Casamento de impedância;. 6. Automação.. I. Conci Kubrusly, Alan. II. Suzano Medeiros, Vivian. III. Pontifícia Universidade Católica do Rio de Janeiro. Departamento de Engenharia Elétrica. IV. Título.

CDD: 620.11

Acknowledgments

Firstly, I would like to thank my advisors Alan Kubrusly and Vivian Suzano for their time and attention, for their patience, support, and all teachings.

I am grateful to my mother and all the support she has given me. Especially for the care and encouragement in my education throughout my life.

I would like to thank all my friends and colleagues for all the essential support, whether directly related to work or not.

I thank the team at CPTI, who helped me through many challenges, especially Lucas, Pedro, Raphael, Rodrigo, and Deivyd.

Finally, I would like to express my gratitude to PUC-Rio for the opportunity to become a Master of Science in Electrical Engineering. This study was financed in part by the Coordenação de Aperfeiçoamento de Pessoal de Nível Superior - Brasil (CAPES) - Finance Code 001 and by FAPERJ Master's Degree scholarship.

Abstract

Torres de Sousa Andrade, João Pedro; Conci Kubrusly, Alan (Advisor); Suzano Medeiros, Vivian (Co-Advisor). **Development and assessment of a simplified automatic impedance matching network for electromagnetic acoustic transducers.**. Rio de Janeiro, 2023. 68p. Dissertação de Mestrado – Departamento de Engenharia Elétrica, Pontifícia Universidade Católica do Rio de Janeiro.

Ultrasonic waves can be used for nondestructive testing. They are generated and acquired by transducers. Electromagnetic acoustic transducers (EMATs) have some advantages over traditional piezoelectric transducers. Mainly, the ability to generate ultrasonic waves without requiring physical contact with the medium under test. Nevertheless, they present a main drawback of less efficiency, which leads to a lower signal-to-noise ratio. To overcome this, impedance matching techniques can be used. The L-network impedance matching network is often used in order to ensure maximum power transfer to the EMAT from the excitation electronics. There is a wide range of variables that can affect an EMAT's impedance besides the transducer itself, namely, the properties and distance to the specimen material, the temperature, and the excitation frequency. Therefore, to ensure optimal power transfer, the L-network's configuration needs to be tuned whenever one of the factors that affect impedance changes. The process of manually adjusting the impedance matching network is a laborious and time-consuming task, therefore, its automation can be of great benefit to the use of EMAT transducers. In this work, a simplified one-element automatic matching network is proposed. The theoretical optimal values for the one-element matching networks are derived. Simulations confirmed their effectiveness to increase EMAT efficiency. Manual and automatic networks were designed and built. Experiments were performed with two different EMATs at several frequencies. The automatic system was able to determine the best configuration for the one-element matching network and provided up to 5.6 dB gain, similar to the manual solution. The automatic setup was more than two-fold faster than the manual one.

Keywords

Electromagnetic Acoustic Transducers; Nondestructive testing; Impedance Matching; Automation.

Resumo

Torres de Sousa Andrade, João Pedro; Conci Kubrusly, Alan; Suzano Medeiros, Vivian. **Desenvolvimento e avaliação de uma rede de casamento de impedância simplificada automática para transdutores acústicos eletromagnéticos.**. Rio de Janeiro, 2023. 68p. Dissertação de Mestrado – Departamento de Engenharia Elétrica, Pontifícia Universidade Católica do Rio de Janeiro.

Ondas ultrassônicas podem ser usadas para ensaios não destrutivos. Elas são geradas e adquiridas por transdutores. Transdutores acústicos eletromagnéticos (EMATs) possuem algumas vantagens em relação a transdutores tradicionais piezoelétricos, principalmente a capacidade de gerar ondas ultrassônicas sem necessidade de contato físico com o meio em teste. No entanto, sua principal desvantagem é a menor eficiência, que resulta em uma relação sinal-ruído mais baixa. Técnicas de casamento de impedância podem ser utilizadas para combater isso. A rede de casamento de impedância do tipo circuito L é comumente utilizada para garantir a transferência máxima de potência da eletrônica de excitação para o EMAT. Existem diversas variáveis que podem afetar a impedância de um EMAT além do próprio transdutor, como as propriedades e distância do material, a temperatura e a frequência de excitação. Portanto, para garantir a transferência máxima de potência, o circuito de casamento de impedância precisa ser reconfigurado e ter seus valores ajustados sempre que um dos fatores mencionados acima sofrer alteração. O processo de ajuste manual desta rede é trabalhoso e demorado, portanto, sua automação pode trazer grandes benefícios para o uso de transdutores EMAT. Esta dissertação propõe um circuito simplificado, com um único elemento, para casamento de impedância de EMATs. Os valores teóricos ideais para circuitos mono-elemento foram obtidos. Simulações confirmaram sua viabilidade em aumentar a eficiência do EMAT. Circuitos de casamento manual e automáticos foram projetados e construídas. Configurações experimentais foram elaboradas e postas em prática. Experimentos com dois transdutores EMATs distintos foram conduzidos utilizando várias frequências. O sistema automático foi capaz de determinar a melhor configuração para o circuito mono-elemento de casamento de impedância e forneceu um ganho de até 5,6 dB, similar à solução manual. A configuração automática foi mais de duas vezes mais rápida do que a manual.

Palavras-chave

Transdutores Acústicos Eletromagnéticos; Ensaios Não destrutivos; Casamento de impedância; Automação.

Table of contents

List of figures

List of tables

1
Introduction

Ultrasonic waves are widely used in nondestructive testing [1, 2]. In order to generate ultrasonic waves, different types of transducers can be used, the most common one being the piezoelectric [3]. These transducers require direct contact with the medium under test, either bonded or through a coupling medium, to operate [3–5]. They can easily generate P waves, however, their use to generate S waves is not straightforward [6, 7].

Electromagnetic acoustic transducers (EMATs) have some advantages when compared to traditional piezoelectric transducers. They are capable of generating various types of ultrasonic waves and polarizations in conductive materials without contact [3,8–10]. These advantages yield from the transducer's working principle. EMATs can have three coupling mechanisms, namely, Lorentz force, magnetization force, and magnetostriction. They generally consist of a coil underneath a permanent magnet or a permanent magnet array, although an electromagnet can also be used. The current applied to the coil induces a current density in a conductive medium skin-depth [3]. The interaction between the induced current density and the magnetic field produced by the permanent magnet generates a Lorentz force field within the object. Due to the external magnetic field, a magnetization force can also be generated in ferrous objects. The magnetic field can also cause a dimensional change or magnetostriction. These forces contribute to generating ultrasonic waves inside the medium [3].

Many of the factors which affect the EMATs impedance also yield from the EMATs construction. Not only the coil geometry affects its impedance, but also the distance from the coil to the magnet as explored by Wu et al. [11]. The transducer can also possess a backplate between these components that also affects its impedance, as exposed by Wang. et al [12]. Beyond the EMAT itself, the distance from it to a ferrous material, so-called 'lift-off', also affects the transducer's impedance [13], and so does the temperature [14]. Finally, the excitation frequency affects the EMAT's impedance as well.

The main drawback of EMATs is their low efficiency. Consequently, they have a lower signal-to-noise ratio (SNR) than piezoelectric transducers, which can hinder the use of EMATs [11, 13]. One way to alleviate this shortcoming is to guarantee the maximum power transmission from the excitation electronics to the transducer [14,15]. The maximum power transference theorem states that whenever the electric input impedance of the transducer equals the complex conjugate of the output impedance of the pulser, maximum power is transferred to the transducer [16]. The pulser's output impedance is usually fixed. The transducer impedance, however, depends on a wide variety of factors. Therefore, impedance matching is usually designed for a specific EMAT and operating frequency [8, 17].

One common way to impedance-match EMATs is to use the L-network, which is a circuit composed of two reactive lumped elements, each one can be either an inductor or a capacitor [18]. However, to be able to impedance-match, the inductance or capacitance values of the network's components depend on the pulser and transducer impedances. Because the EMAT impedance is generally not previously known, as it depends on various factors, the impedance matching process usually consists of sweeping for the network's configurations that provide the maximum signal amplitude [14]. Manually adjusting these configurations is a time-consuming process and subject to human interpretability and errors. Therefore, automation of this process can be of great benefit to EMAT-based inspection systems, not only for time savings reasons but also to ensure optimal operation.

Some works which aim to improve EMAT performance study the effects of physical changes in the transducers. Wu et al. [11] studied the effect of magnet-to-Coil distance on the performance characteristics of EMATs, concluding the magnet-to-coil distance affects the magnetic flux density and eddy current density at the medium's surface and that, for a specific EMAT, there is an optimal magnet-to-coil distance that maximized its conversion efficiency over a range of lift-off distances. Wang et al. [12] explored the effects a copper backplate, positioned between the coil and magnet at various distances from the coil, can have on the EMAT impedance and the received pulse width and amplitude of thickness-measurement signals. An equivalent circuit model of the receiving coil–backplate structure was established and used to predict these effects. Ding et al. [13] measured and confirmed the effect of lift-off on EMAT impedance. Although the term 'impedance matching' was not mentioned, a resonant capacitor was proposed to enhance the lift-off performance of the receiving EMAT. This resonant capacitor proved effective and is very similar to the one-parallel-element matching network explored in this thesis. Zao et al. [14] explored the variation of EMAT impedance with different temperatures. An automatic solution, based on L-network impedance matching, was developed to enhance signal amplitude.

These four works [11–14], each explore the effects that one variable can have on EMAT performance, namely, the magnet-to-coil distance, the backplate distance, lift-off, and temperature. In contrast, Jian et al [19] explored the effects of various variables on EMAT impedance, namely, coil geometry and size, different materials samples, and various lift-off distances. It was concluded that "an EMAT must be considered as a system, including a pulse generator, a transmitting coil, and a metal sample", elements that can affect the equivalent inductance of the transducer. Jian et al. [19] however, did not explore any techniques to improve EMAT performance.

Kuang et al. [17] explored an automated system, that measures the impedance of high power piezoelectric transducers in real time, relying on the analysis of amplitude and phase of both voltage and current across the transducer. The system achieved resonance tracking with a phase-locked loop by modulation of the excitation frequency. This method, however, is much more elaborate, requiring higher-cost electronics and more complex software than impedance matching using an L-network. Furthermore, an arbitrary excitation frequency cannot be chosen when using this system.

1.1 Thesis Contributions

The automated impedance matching process, which searches for the maximum signal amplitude, is capable of taking various factors into consideration at once, optimizing the EMAT system.

In this thesis, simplified impedance matching networks are proposed, their theoretical values are derived, and their viability for improving EMAT performance is explored. A method for measuring EMAT impedance by using such networks is also proposed.

Automatic one-parallel-element networks are built, tested, and compared to their manual counterpart. Unlike Zao et al. [14], their application by using different transducers at different excitation frequencies is explored, confirming the use of automated impedance matching networks as a means to improve EMAT performance with respect to the change of more than one variable.

1.2 Dissertation Structure

The remainder of this dissertation is organized as follows:

Chapter 2 presents the background theory employed in the subsequent sections. The types of ultrasonic wave polarization are defined and their use in nondestructive testing are described. Conventional piezoelectric transducers are mentioned and compared to EMATs. Spiral coil EMATs are thoroughly discussed. The electronics needed for an ultrasonic inspection system are also presented. Finally, the maximum power transfer theorem is stated.

Chapter 3 presents the impedance matching networks analyzed. The L-matching network is discussed, and its theoretical values are shown. Two simplified one-element networks are proposed. Its optimal values are derived. Finally, some comments are made on how to find the network values in practice, without prior knowledge of the load's impedance.

Chapter 4 presents an analysis of EMAT impedance. Experimental data on different transducers is reported. For some transducers, the evaluation was also performed in varied proximity to ferrous objects.

Chapter 5 presents numerical simulation methods for the circuit which includes source, matching network, and load. LTSpice and Matlab models were developed and compared.

Chapter 6 presents the matching networks that were built and the different experimental setups which used them. Three networks are described, a manual one, a preliminary automatic, and a final automatic network built on a custom-made PCB. The experimental setups are explained concerning all the equipment used.

Chapter 7 presents the experimental results for each of the experimental setups with various comparisons between results for different frequencies, transducers, and the simulations performed previously.

Chapter 8 concludes this thesis and presents plans for future work.

1.3 Publication

From part of the work presented in this dissertation, a paper was published in the International Symposium on Instrumentation Systems Circuits and Transducers, INSCIT 2023, namely,

J. P. Andrade, V. S. Medeiros, and A. C. Kubrusly, "A simplified automatic impedance matching network for electromagnetic acoustic transducers", 2023 International Symposium on Instrumentation Systems Circuits and Transducers (INSCIT), 2023.

2
Background Theory

In this chapter, the background theory that is needed for further chapters is exposed. Ultrasonic waves are presented and their use in nondestructive testing is described. EMATs are described and compared to traditional piezoelectric transducers. EMATs of the spiral-coil type, used in this work, are modeled. The excitation electronics needed for an ultrasonic inspection system are also described. Finally, the maximum power transfer theorem is stated.

2.1
Ultrasonic waves and transducers

Ultrasonic waves are mechanical waves that propagate through fluid or solid mediums, with a higher frequency than humans can hear [5]. In solids, ultrasonic waves can be split into two categories with respect to their particle motion direction. Primary (P) or longitudinal waves have the particles of the medium move in the same direction as the propagation of the wave. In Secondary (S) or transversal waves, the particles move perpendicular to the wave's propagation, they can also be further divided into shear horizontal (SH) and shear vertical (SV) waves [20]. Because fluids cannot withstand shear motion, S waves can only propagate across solid mediums. It is also worth mentioning that it is possible to have ultrasound propagating in both modes simultaneously, though this is generally avoided in inspection systems. P and S waves propagate through the medium at different speeds [20, 21], namely c_L and c_T respectively, which are given by:

$$c_L = \sqrt{\frac{\lambda + 2\mu}{\rho}} \tag{2-1}$$

and

$$c_T = \sqrt{\frac{\mu}{\rho}} \tag{2-2}$$

where ρ is the medium's density, λ is the first Lamé parameter, and μ is the second Lamé parameter [21, 22].

When propagating through non-ideal media, ultrasonic waves are attenuated, not only because of intrinsic thermal and viscous effects but also because of any impurities and imperfections in the medium [1]. When propagating across an interface between two media reflection and refraction occur depending on both medium's properties and the incident angle. It is also possible for a wave to change modes when reflecting or refracting [5]. To both generate and capture an ultrasonic wave, a transducer and its accompanying electronics are required. A transducer can be broadly defined as "a device that transforms energy from one domain into another" [23]. Here, the transducer converts energy between mechanical waves, or sound, to electrical signals and vice-versa [1, 24].

2.2 Nondestructive testing

Nondestructive testing (NDT) can generally be defined as an examination, test, or evaluation performed on a test object without changing or altering that object [25]. It can be performed to assess the object's condition, usefulness, or serviceability and conditions that affect service life. NDT or nondestructive evaluation (NDE) may also be used to measure various object characteristics, such as size, dimension, discontinuities, structure, including hardness, and grain size, among others [25].

Ultrasonic waves can be used in NDT and inspection systems [1]. There are three main types of setups used in NDT, namely, Pulse-Echo, Pitch-Catch, and Through-Transmission [1]. These three setup types are represented in Fig. 2.1. A Pulse-Echo Setup uses only one transducer, acting as both transmitter and receiver of ultrasound waves. Both Pitch-Catch and Through-Transmission setups use two transducers, one acting as a transmitter and the other acting as a receiver. The difference lies in their positioning relative to one another. In the Pitch-Catch setup, the transducers are not aligned, meaning the ultrasonic waves need to scatter or reflect in order to reach the receiver from the transmitter. In a through-transmission setup, both transducers are aligned at opposite ends of the medium. The analysis of the wave propagation through the medium yields its the measured characteristics. For example, the time between the emission and reception of corresponding signals in the trough transmission setups is the time the ultrasound takes to propagate across the thickness of the medium. This thickness can be calculated from the time and the corresponding wave speed. A flaw can be detected as it generates an echo that is received in a different time interval than the medium boundary's echo [1].

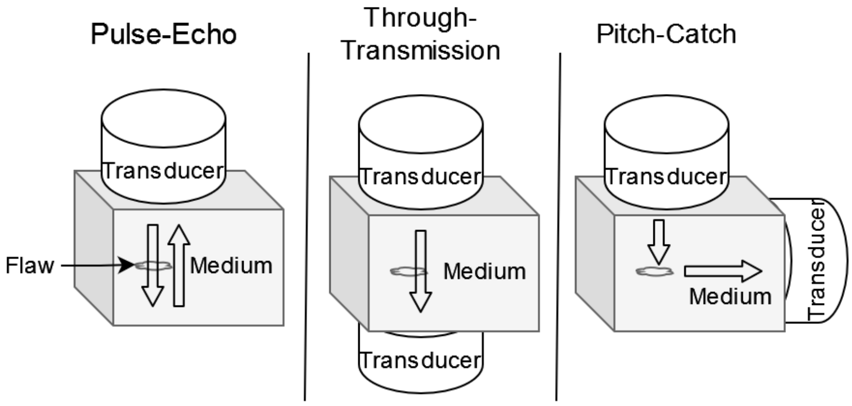

Figure 2.1: Representation of the three main types of ultrasonic system setups, namely, Pulse-Echo, Through-Transmission, and Pitch-Catch, respectively from left to right.

2.3 Traditional Piezoelectric transducers

Traditional Piezoelectric transducers work based on the principle that, when certain materials, such as some crystals or ceramics, for example, are deformed, a voltage across the material is created due to the material's crystalline structure [22]. The reverse is also true, when a voltage or electric field is applied to piezoelectric materials, the materials internal forces change, causing a deformation. This principle fits the definition of a transducer, converting electric into mechanical energy and vice-versa. The word piezoelectric, derived from ancient Greek, means electricity resulting from pressure [22, 26].

This type of transducer can be efficient in this energy conversion [27]. However, the electric signal is converted into a deformation in the material of the transducer itself. Therefore, for this mechanical energy to be transferred to the test object, contact between the transducer and the medium is needed [1]. Water or gel is commonly used as a couplant for this transmission. However, as has been established, fluids do not propagate shear waves. Therefore, to generate S waves, the transducer needs to be bonded to the medium, or a conversion of mode in refraction is used [1].

2.4 EMAT transducers

Electromagnetic Acoustic Transducers work by a completely different principle. EMATs consist of a coil underneath a permanent magnet, permanent magnet array, or electromagnet. When a current is injected into the coil, it induces a current density in the skin-depth of a conductive medium [3]. The permanent magnet generates a magnetic field that penetrates into the medium.

The interaction between the current density and the magnetic field generates a Lorentz force field on the surface of the medium that is given by the cross product

$$F = J \times B \tag{2-3}$$

where J is the current density, B is the magnetic field, and F is the resulting Lorentz force field, which, in turn, can generate ultrasonic waves directly inside the medium [3, 28]. Therefore, EMATs do not need physical contact with the medium, which is a significant advantage over traditional transducers [3, 12, 28]. Furthermore, depending on the magnet and coil arrangement, different types and polarization of ultrasonic waves can be generated [8–10].

There are many types of EMATs that use varied arrangements of coils and permanent magnets [3]. In this work, only spiral-coil EMATs are used.

2.4.1 Spiral Coil EMAT and circuit modeling

Spiral-coil EMATs are one of the most basic types of EMATs and are often used [3]. They have a single permanent magnet, oriented perpendicular to the medium's boundary, meaning the magnetic field below the EMAT is mostly perpendicular to the conductive material's surface. They also use a spiral-coil, which means that the current density generated is oriented circumferentially. The resulting Lorentz force generates a radial-polarized S wave beneath the EMAT [3, 10]. Fig. 2.2(a) shows a schematic representation of a spiral-coil of EMAT. Since the main electric element of an EMAT is a coil, a simplified lumped-element model for an EMAT consists of an inductor in series with a resistor [10, 13]. Fig. 2.2(b) shows this model.

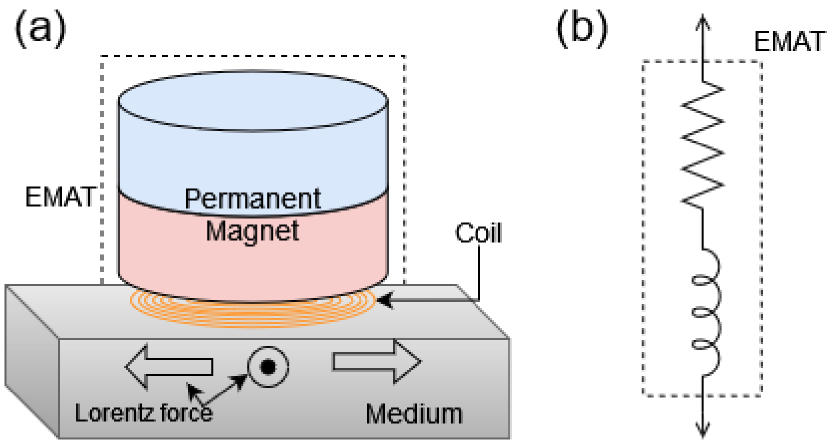

Figure 2.2: Spiral-coil EMAT. (a) Physical representation of an EMAT consisting of a spiral-coil underneath a cylindrical permanent magnet. The red section of the magnet indicates the north pole, and the blue section indicates the magnet's south pole. Both components are usually enclosed in a casing. The Lorentz forces generated are indicated by arrows inside the medium. (b) Simplified model consisting of a resistor in series with an inductor.

2.5 Excitation Electronics

Besides the transducer, the electronics are also very important in an ultrasonic-based inspection system, these can be referred to as 'pulse-receiver' [1]. The pulser which drives the system, is responsible for generating the high-voltage signal that goes into the EMAT. This pulser can be modeled as a source, with an internal output impedance. Usually, the output impedance, Z_i, is equal to 50 Ω in most laboratory equipment [29]. A representation of the pulser model is shown in Fig. 2.3. The receiver is responsible for amplifying the electric signal generated by the transducer when an ultrasonic wave is captured so it can be acquired by an oscilloscope [1].

2.6 Maximum power transfer theorem

A model of a pulser connected to a generic load is shown in Fig. 2.3. The power over the load is given by

$$P_0 = I_{rms}^2 R_0 = \frac{|V_s|^2}{2} \frac{R_0}{(R_i + R_0)^2 + (X_i + X_0)^2}, \tag{2-4}$$

where I_{rms} is the root mean square current over the load. Z_i is the source's output impedance, that can be decomposed by its resistance R_i and reactance X_i. Z_0 is the load impedance, that can be decomposed by its resistance and reactance, respectively R_0 and X_0. V_s is the voltage value of the source. For

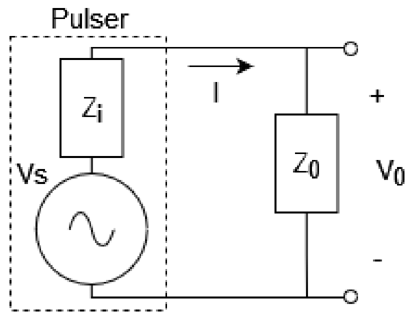

Figure 2.3: Circuit where AC power is transferred from the source with magnitude V_s and internal impedance Z_i to a load of impedance Z_0. The voltage and current across the load are V_0 and I respectively.

a given V_s and Z_i, to maximize power P_0, Z_0 needs to maximize the fraction $\frac{R_0}{(R_i+R_0)^2+(X_i+X_0)^2}$. For each value of R_0, there is a minimum in the denominator when $(X_i + X_0) = 0$, therefore we have:

$$X_0 = -X_i. \tag{2-5}$$

Considering Eq. (2-5), Eq. (2-4) becomes

$$P_0 = \frac{|V_s|^2}{2} \frac{R_0}{R_0^2 + 2R_iR_0 + R_i^2}. \tag{2-6}$$

To find its maximum one has:

$$\frac{\partial P_0}{\partial R_0} = \frac{|V_s|^2}{2} \frac{-R_0 + R_i}{(R_0 + R_i)^3} = 0 \tag{2-7}$$

which yields

$$R_0 = R_i. \tag{2-8}$$

From Eq. (2-5) and Eq. (2-8) one has:

$$Z_o = Z_i^*, \tag{2-9}$$

where the asterisk means the complex conjugate. Therefore, the maximum power transfer theorem states that whenever the input impedance of a load equals the complex conjugate of the source output impedance maximum power is transferred to the load [16, 18]. Assuming the source impedance as purely real, that is, a resistance, the maximum power transfer occurs when the load impedance and the source resistance are equal.

In this thesis, the load is the EMAT, whose impedance value generally differs from the source output impedance. For this reason, one has to use some matching technique to achieve maximum power transfer [14].

3
Impedance Matching Techniques

As stated in Section 2.6, to achieve maximum transferred power, one has to use some impedance matching technique. In this chapter, the most common and simplified ones are presented.

3.1
L-Networks

One of the simplest and most commonly used topologies for impedance matching is the L-network, which uses two lumped elements [18] that are associated with the load, changing the equivalent impedance seen by the source. To introduce a lossless network, reactive elements are required. Thus, each element can be either a capacitor or an inductor. There are two possible layouts, as shown in Fig. 3.1. Hence, considering all possible combinations of elements, there are eight distinct possibilities for the matching L-network circuit, not all of them are capable of perfectly matching any load to any source [18]. If the load resistance is greater than the source impedance, then the circuit in Fig.3.1(a) should be used as the matching network. Otherwise, one should use the circuit in Fig.3.1(b) [18].

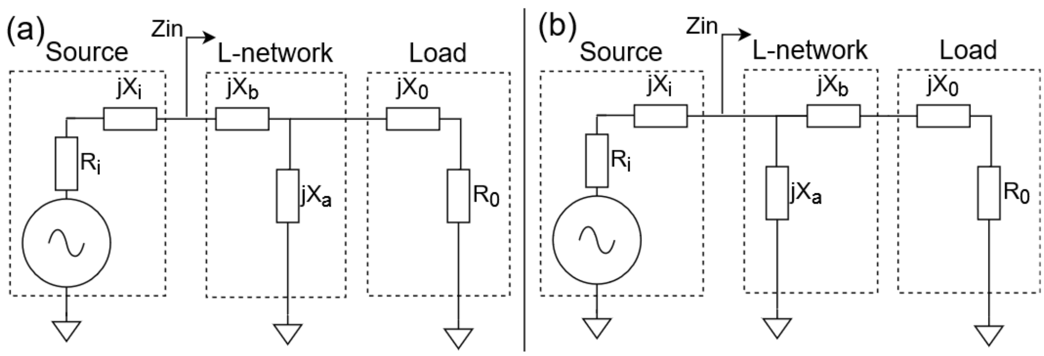

Figure 3.1: L-section matching networks. (a) Recommended network for $R_0 > Z_i$, (b) Recommended network for $R_0 < Z_i$. Where R_i and X_i are the resistance and reactance of the source, respectively, and R_0 and X_0 are the resistance and reactance of the load, respectively. The reactances X_a and X_b are the elements of the L-network. Here, the load represents the EMAT. Z_{in} indicates the impedance association of the L-network and the load, as seen by the source.

The EMAT impedance is explored in detail in the next chapter, but for now, it is worth commenting that, generally, it has lower resistances than the usual 50 Ω of the source. Therefore, the circuit shown in Fig. 3.1(b) is adopted from here on.

The theoretical values for the reactances X_a and X_b of the L-network matching layer in Fig. 2.2(b) that ensure impedance matching and therefore maximum power transfer to the load are:

$$X_a = \frac{-(R_i^2 + X_i^2)}{QR_i + X_i}, \tag{3-1}$$

$$X_b = QR_0 - X_0, \tag{3-2}$$

where,

$$Q = \pm\sqrt{\frac{R_i(1 + \frac{X_i}{R_i}^2)}{R_0} - 1}. \tag{3-3}$$

Simplifying with the assumed source output impedances, namely $R_i = 50$ Ω and $X_i = 0$ Ω:

$$X_a = \frac{\mp 50}{\sqrt{\frac{50}{R_0} - 1}}, \tag{3-4}$$

$$X_b = \pm R_0\sqrt{\frac{50}{R_0} - 1} - X_0. \tag{3-5}$$

where the symbol ± refers to the sign that should be taken according to the two possible values that Q can assume, either positive or negative. When Q is positive, then X_a is negative; therefore, it consists of a capacitor. In this case, X_b can be either positive or negative depending on the EMAT's impedance Z_0. If Q is negative, then X_a is positive, that is, it consists of an inductor.

Here, Q will always be chosen positive, yielding the following component values:

$$C_a = \frac{-1}{2\pi f X_a}, \tag{3-6}$$

and

$$C_b = \frac{-1}{2\pi f X_b}, \tag{3-7}$$

or,

$$L_b = \frac{X_b}{2\pi f}, \tag{3-8}$$

where C_a is the capacitance of the element X_a, C_b is the capacitance of the element X_b when $X_b < 0$, L_b is the inductance of the element X_b when $X_b > 0$, and f is the frequency.

The condition for $X_b < 0$ is:

$$X_0 > R_0\sqrt{\frac{50}{R_0} - 1} \tag{3-9}$$

As such, it is possible to use only capacitors for the L-network when the resistance of an EMAT is relatively low compared to its reactance. This condition is also more easily fulfilled at higher frequencies. Taking into account the EMAT circuit model presented in Section 2.4.1 the impedance is proportional to the frequency, but the resistance is constant.

When building the matching network, capacitors are better compared to inductors because they are easier to source [30], especially for the high power requirements of an EMAT system. They also associate by addition in parallel [31], meaning that having a bank with binary weights only needs simpler single pole single throw (SPST) switches or relays, in comparison with the double pole single throw (DPST) switches for inductors association in series.

It is also worth mentioning that, considering $R_0 < Z_i$, the choice of the circuit (b) in Fig. 3.1 guarantees that all the equations from (3-1) to (3-9) result in a purely real value. If the condition is switched, it is possible to find the matching network values for the circuit in Fig. 3.1 (a) simply by switching around the load and source's impedances in equations (3-1) to (3-3) [32]. Switching the values in the equations would be equivalent to switching the connections to the matching network in the circuit, it is possible to see in Fig. 3.1 that doing so would change from the circuit in (a) to (b) and vice-versa.

3.2 Simplified One-Parallel-Element (X_a)

Here it is investigated a simplified one-element matching network. This network consists of removing the element X_b from the circuit shown in Fig. 3.1(b), keeping only X_a in parallel with the load. The resulting circuit is shown in Fig. 3.2. With the impedance of only one-element to be adjusted, it is impossible to achieve the two degrees of freedom required to perfectly match the source and the load impedance and optimize the power transferred to the load. However, one still can find the best possible value for X_a. That is, the value for X_a that maximizes the power transferred to the load under this condition.

The power provided by the source is given by

$$P = \frac{|V|^2 Z_{in}}{2|Z_{in} + R_i|^2}, \tag{3-10}$$

where $|V|^2$ is the absolute squared value of source voltage and Z_{in} is the impedance prior to the matching network, as highlighted in Fig. 3.2, that is

$$\frac{1}{Z_{in}} = \frac{1}{jX_a} + \frac{1}{R_0 + jX_0}, \tag{3-11}$$

where $j = \sqrt{-1}$. Applying Eq. (3-11) into Eq. (3-10), for $X_i = 0$, with some

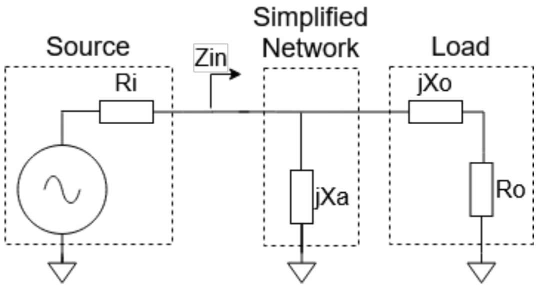

Figure 3.2: Simplified, one-parallel-element matching network, where the impedance of the source is assumed real and composed only by a resistance R_i. The load impedance is $R_0 + jX_0$, where R_0 and X_0 are the resistance and reactance of the load. The reactance X_a is the single element within the simplified matching network. Here, the load represents the EMAT. The parallel association between the simplified network and the load has total impedance Z_{in}.

manipulation, leads to

$$P = -\frac{1}{2}\mathcal{I}\left\{\frac{V^2 X_a(R_0 + jX_0)}{(R_i + \frac{X_a j(R_0+jX_0)}{\xi})(R_i + \frac{X_a j(R_0-jX_0)}{-R_0+jX_0+jX_a})\xi}\right\} \tag{3-12}$$

where $\mathcal{I}$ indicates the imaginary part of what is inside the brackets, and

$$\xi = R_0 + jX_0 + jX_a. \tag{3-13}$$

Because the matching network consists of reactive elements only, it does not dissipate power. Hence, maximizing the source power also maximizes the power delivered to the load, that is, the EMAT. Therefore, from

$$\frac{\partial P}{\partial X_a} = 0 \tag{3-14}$$

one has

$$X_a = -\frac{R_0^2 + X_0^2}{X_0}. \tag{3-15}$$

Note that X_a does not depend on the resistance of the source, as long as X_i is zero. Following the model in section 2.4.1, an EMAT has positive values for its resistance and reactance; therefore, the optimal value for the simplified single parallel element is negative, meaning that X_a should be a capacitor, no matter the specific load values.

3.3 Simplified One-Series-Element (X_b)

Another possible simplification of the full L-network is to remove X_a, leaving only X_b in series with the load. The power provided by the source follows Eq. (3-10), where Z_{in} in this configuration is:

$$Z_{in} = jX_b + R_0 + jX_0. \tag{3-16}$$

Applying Eq.(3-16) into Eq.(3-10), for $X_i = 0$, with some manipulation, leads to

$$P = \frac{(X_b + X_0)\frac{(R_i+R_0)(X_b+X_0)+R_0(X_b+X_0)}{\eta}}{2\eta} - \frac{(R_i + R_0)(\frac{(X_b+X_0)^2-R_0(R_i+R_0)}{\eta})}{2\eta} \tag{3-17}$$

where

$$\eta = (R_i + R_0)^2 + (X_b + X_0)^2. \tag{3-18}$$

Following the same logic as in the previous section, from

$$\frac{\partial P}{\partial X_b} = 0 \tag{3-19}$$

one has

$$X_b = -X_0. \tag{3-20}$$

Note that X_b only cancels out the imaginary part of the load's impedance. This means that the one-parallel-element network consists of a capacitor.

3.4
How to find the matching network's values in practice

In practice, the values for the matching network are usually not determined using the aforementioned equations presented in the previous sections. This is because the load impedance is not known a priori, and to measure it, it is necessary to use an impedance analyzer. Furthermore, as mentioned in previous sections, this value can change with a wide variety of factors.

The practical approach consists of changing the network values X_a and/or X_b and observing the effect of the change on the power transmission. In a laboratory environment, this usually consists of an EMAT system with a matching network that can be manually adjusted, by flipping switches, for example. This system is connected to a oscilloscope meaning that if the configuration of the network is changed, the resultant signal can be observed to check for improvement or worsening. Therefore, a simple process of testing configurations, until the best one is found, can be employed.

3.4.1
For one-element networks

For a one-element network, the worst case is to perform the same number of measurements as there are configurations in the matching network. For example, consider a bank of eight individually switchable capacitances. This would result in 256 possible configurations. This is the same for both one-element networks explored previously.

It is also worth mentioning that knowing the expected format of the power output as a function of the matching network's values can help in this process, as it is possible to devise a more clever search algorithm than just sweeping all possibilities. As shown the next sections, this function has only one local maximum, making many search algorithms feasible.

3.4.2
For full L-networks

The full network has two degrees of freedom, which means a whole plane of possibilities. Using the same example as before, with two banks of eight capacitors each, in the worst-case scenario, a full sweep now has 256x256 or 65536 measurements needed. There is, however, a better way to find both values relying on using the full L-network as two simplified one-element networks.

If X_a is set to zero, it is possible to find the optimal empiric X_b for a one-series-element network, that is $X_{b_{emp}}$, by switching all the possible values for X_b. The same is true for the other one-element network, that is, by setting X_b to zero and sweeping X_a, one can find the optimal empirical value $X_{a_{emp}}$.

In sections 3.3 and 3.2, it has been observed that the optimal values for simplified one-elements are not the same as the ones for the full network. However, in possession of the analytical solutions calculated for the optimal one-element networks in Eq. (3-15) and Eq. (3-20), it is possible to get inverse relationships and calculate the load impedance. This can be done as follows, with both the empirical values found for the optimal X_a and X_b, that is $X_{a_{emp}}$ and $X_{b_{emp}}$, Eq. (3-21) and Eq. (3-22) can be used to find $X_{0_{emp}}$, and $R_{0_{emp}}$, respectively, the empirical reactance and resistance of the transducer. Those are,

$$X_{0_{emp}} = -X_{b_{emp}} \tag{3-21}$$

and

$$R_{0_{emp}} = \sqrt{X_{b_{emp}}(X_{a_{emp}} - X_{b_{emp}})} \tag{3-22}$$

It is worth mentioning that $R_{0_{emp}}$ is a real number. As we can see comparing the results from Eq. (3-15) and Eq. (3-20), X_a is greater than X_b. The same follows for the empirical values. Assuming that we find $R_{0_{emp}} < 50$, then we apply the resulting values of Eq. (3-21) and Eq. (3-22) in Eq. (3-4) and Eq. (3-5). Note that this method only requires two one-dimensional sweeps, one for each reactive element. Therefore, for the example of two banks of eight capacitors, this method improves the required measurements from 256^2 to 256x2, which means a 128-time improvement.

4
EMAT impedance analyses

In order to evaluate and compare the impedance matching networks mentioned in Section 3, numerical simulations were performed. First, the EMAT's impedance values are needed. In this work, two different spiral-coil EMAT models are used. The first is incorporated in a Ritec RPDR-1000 OEM module, the second is a Sonemat EMAT model HWS2225. An impedance analyzer (Agilent model 4294A) was used to measure the impedance of all transducers by means of a frequency sweep. As mentioned before in Chapter 1, the proximity to ferrous objects affects the EMAT impedance; therefore, the measurements were performed in two conditions: far from any ferrous medium and magnetically attached to a 12 mm steel block, the same used in the forthcoming experimental setup. Additionally, two transducers of the same model, from the RPDR module, were evaluated so that construction differences could be compared. The measurements are shown in Fig. 4.1.

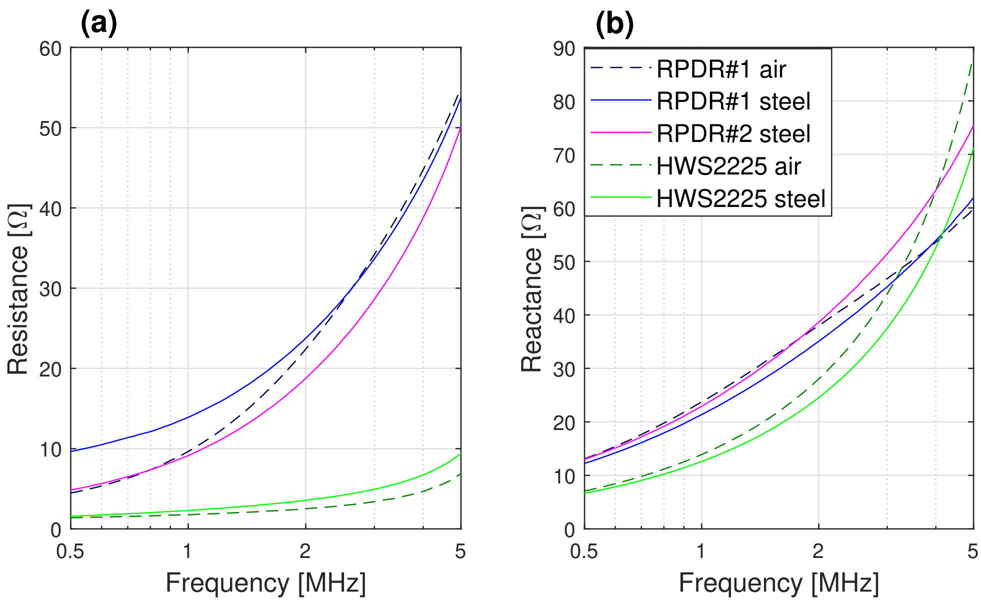

Figure 4.1: (a) real and (b) imaginary parts of the impedance of the EMATs as a function of frequency. Brighter solid lines were measured with the transducers close to a ferrous object and darker dashed lines with them in the air, far from any ferrous object. Blue lines are the measurements for the first RPDR's included EMAT, and magenta for the second one. Green lines are the measurements for the HWS2225 EMAT.

Observing Fig.4.1, one can see that both models of transducers generally have higher resistance and lower reactance when near a ferrous object. For the RPDR's EMAT, however, the resistance varies more with frequency. It is also possible to notice not only the large difference between the two models of transducers but also the considerable difference between two samples of the same model, namely the first and second RPDR-EMAT.

Following the simplified EMAT model found in Chapter 2, the transducer can be modeled as a resistor in series with an inductor. Therefore, the resistance should be constant with frequency and the reactance should behave linearly with frequency. However, as per Fig. 4.1 this is not the case; the resistance varies with frequency in both RPDR EMATs. Because of this, it is convenient to evaluate the EMATs impedance around an intended frequency, where it can be directly translated to resistance and inductance values. The equivalent values of resistance and inductance at 1, 2, 3, and 4 MHz for the EMATs when in contact with the steel sample are reported in Table **??**. These values can be used as input into an electronic simulation program in order to model an EMAT around a frequency of interest.

Table 4.1: Equivalent values found for R+L EMAT model at given frequencies, namely 1, 2, 3, and 4 MHz. The measurements were made with the transducers close to a steel block.

Frequency	HWS2225 R_0	HWS2225 L_0	RPDR#1 R_0	RPDR#1 L_0	RPDR#2 R_0	RPDR#2 L_0
1MHz	2.2702 Ω	2.008 μH	13.7997 Ω	3.658 μH	9.0335 Ω	3.658 μH
2MHz	3.5276 Ω	1.953 μH	23.4684 Ω	3.088 μH	18.4902 Ω	3.088 μH
3MHz	4.9263 Ω	1.989 μH	33.5095 Ω	2.731 μH	28.4681 Ω	2.731 μH
4MHz	6.5810 Ω	2.083 μH	42.8107 Ω	2.529 μH	38.0720 Ω	2.529 μH

5
Simulations

To evaluate the different matching networks and understand the expected results, several simulations were performed. Firstly the circuit in Fig. 3.1 (b) is replicated in the LTspice and the expected results are confirmed. A Matlab model is then developed, yielding the same results. This model is then expanded to generalize the EMATs impedance over frequency. The full bandwidth of the two models of EMAT is presented for each of the three networks explored in Chapter 3 and for no matching network. The results are analyzed to inform the design of the matching networks build and the experimental setup.

5.1
Simulations using electric circuit simulation software

The first simulations were performed using LTspice, which is a free electronic circuit simulation software that allows users to design and test analog circuits [33, 34]. The chosen circuit concerns the second RPDR's EMAT at an excitation frequency of 2 MHz. The values in Table 4.1 and Eq. (3-4) and Eq. (3-5) are used to calculate X_a and X_b, which equal, $-38.31\ \Omega$ and $-14.66\ \Omega$, respectively. Further using Eq. (3-6) and Eq. (3-7) we find $C_a = 2.077$ nF and $C_b = 5.425$ nF. With these values the circuit shown in Fig. 5.1 (a) was simulated. Three other variations were also simulated, namely, (i) a one-parallel-element network such that the element X_a has the same value as the full L-network; (ii) an optimal one-parallel-element network such that the value X_a is obtained using Eq. (3-15), which results in $X_a = -47.70\ \Omega$ and, consequently, $C_a = 1.668$ nF; and (iii) with no network at all. These circuits are shown in Figs. 5.1(b) to (d), respectively. The source voltage was set to 1 V and its frequency undergoes a sweep around the intended operating frequency of 2 MHz. Results are shown in Fig. 5.2. It is worth mentioning that the EMAT equivalent impedance at 2 MHz is not a good approximation throughout this whole range of frequencies, this issue will be resolved subsequently.

The input impedance of the matching network in association with the load, which is at node A in Fig.5.1, is shown in Fig. 5.2(a) and (b), for its real and imaginary parts respectively. Note that the full L-network (blue line) ensures that the input impedance is equal to R_i, that is, its real part is 50 Ω and its

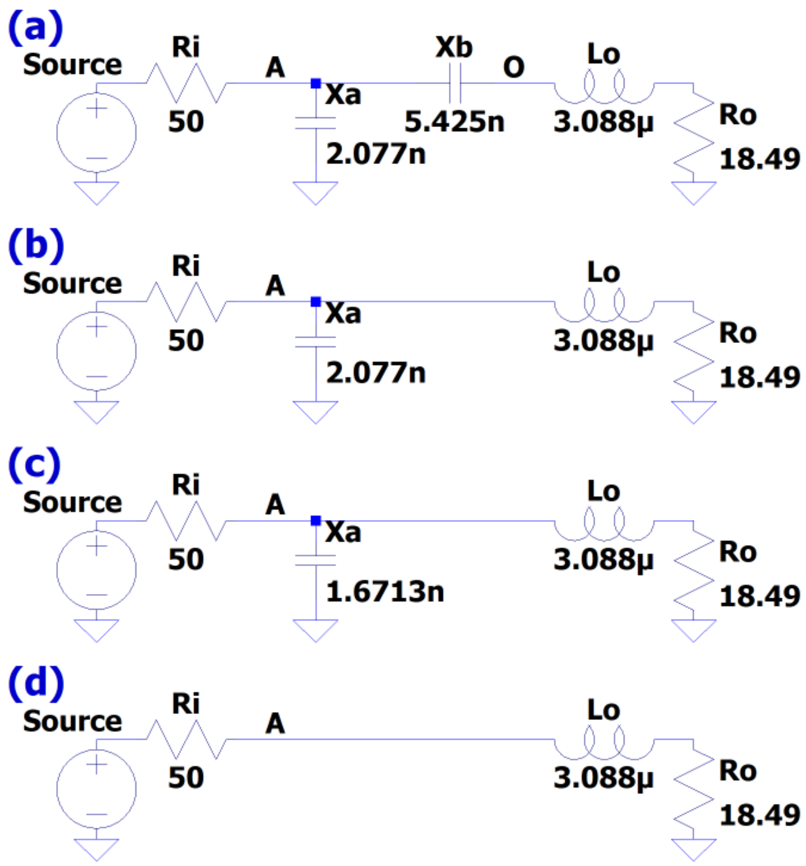

Figure 5.1: Modeled circuits in LTspice. (a) Full L-network, following Fig. 3.1(b); (b) One-parallel-element network with X_a with the same value as the full L-network; (c) one-parallel-element optimal network; and (d) without any network.

imaginary part is null at 2 MHz; therefore, the circuit is indeed matched, while the other networks do not perfectly match the source impedance. Fig. 5.2(c) and (d) show the absolute value for the voltage and power over the EMAT, which is at node O in Fig.5.1 (a) and node A in Fig.5.1 (b) to (d). At 2 MHz, power and voltage are higher with the full L-network (blue line) and lower without any network (purple line). Both one-parallel-element networks present intermediate results, such that the optimal one-parallel-element network (yellow line) presents slightly higher values for both voltage and power compared to the one-parallel-element network with the same X_a as the full L-network (orange line). Note also that the voltage and power behavior are similar for the matched circuits, indicating that monitoring the voltage to obtain its peak value would also lead to the peak value for the power. It is also worth mentioning that the peak power does not occur at 2 MHz, this is because the transducer is inherently more efficient at higher frequencies. These are the best configurations for the 2 MHz excitation frequency.

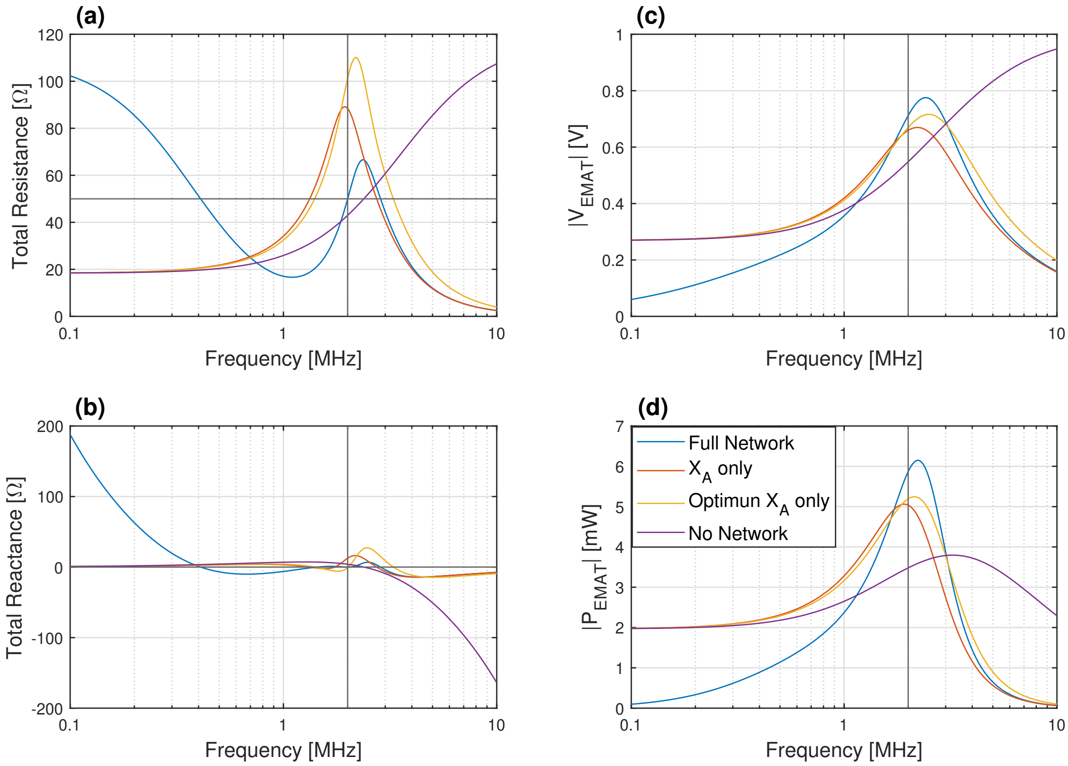

Figure 5.2: Simulations in LTspice for a full L-network are represented by the blue lines, optimal one-parallel-element network are represented by the yellow lines, non-optimal one-parallel-element network by the red lines, and without any network by the purple lines. (a) shows the real part of the input impedance at node A in Fig.5.1, (b) shows the imaginary part of input impedance at node, (c) shows the absolute value of voltage over the EMAT, at node O in Fig.5.1, (d) Absolute value of power over the EMAT, at node O in Fig.5.1.

At the intended operating frequency of 2 MHz, the full network provides a gain of 2.19 dB in voltage across the transducer, compared to the unmatched circuit. The one-element network with the same X_a as the full L-network provides 1.61 dB and the optimal one-parallel-element network provides 1.74 dB improvement. These gains indicate that a simplified one-parallel-element network is feasible for increasing the transferred power, and also, the optimal one-parallel-element network provides a better result than the non-optimal one-element network provides. Therefore, simply using the same value for X_a as the full L-network is not indicated. In this case, the optimal one-parallel-element network provided 90.16 % of the power obtained with the full L-network.

5.2 Theoretical calculations

It is worth mentioning that, using LTspice simulation and data analysis is cumbersome and time-consuming, limiting the number of possible circuits that can be tested. Therefore, a model to compute the aforementioned circuit responses was developed in Matlab aiming to replace the LTspice simulation while providing the same results. The model was formulated as a Matlab function and has X_a, X_b, R_0, and L_0 as input. It assumes the source impedance of 50 Ω and generates a frequency vector of 201 points from 100 kHz to 10MHz, the same span used in both the impedance analyzer measurements and LTspice simulations. It returns the same data as the LTspice simulations, namely, the voltage and current outputs of the source and inputs of the EMAT, respectively, V_{out}, I_{out}, V_{in} and I_{in}. Those are calculated through the transfer function for the voltages and currents that are based on the circuit component's impedance. As the input voltage is normalized, each output has the same value as its transfer function. Eq. (5-1) through (5-6) were used in the model.

The voltage across the source, that is at node A in Fig. 5.1 is given by

$$V_{out} = \frac{Z_{in}}{Z_{in} + Z_{source}}, \tag{5-1}$$

where Z_{source} is the source's impedance, which, in this case, is equal to R_i or 50 Ω. Z_{in} is the impedance of the network and the load as seen by the source, and indicated in Fig. 3.1 and Fig. 3.2. The current through the source, or through R_i in Fig. 5.1 is given by

$$I_{out} = \frac{1}{Z_{in} + Z_{source}}. \tag{5-2}$$

The voltage across the EMAT, that is at node A in Fig. 5.1 (a), and node O in Fig. 5.1 (b) to (d) is given by

$$V_{in} = \frac{Z_0}{Z_0 + Z_b}, \tag{5-3}$$

where Z_0 is the load impedance, calculated by:

$$Z_0 = sX_0 + R_0, \tag{5-4}$$

such that,

$$s = j2\pi f, \tag{5-5}$$

and f is the frequency vector. Finally, the current at the EMAT, or L_0 and R_0 in Fig. 5.1 is given by

$$I_{in} = \frac{V_{in}}{Z_0}. \tag{5-6}$$

In Fig. 5.3 V_{in}, I_{in}, and I_{out} obtained with the data from the Matlab model is reported as black dashed lines, superposed to the equivalent voltages and

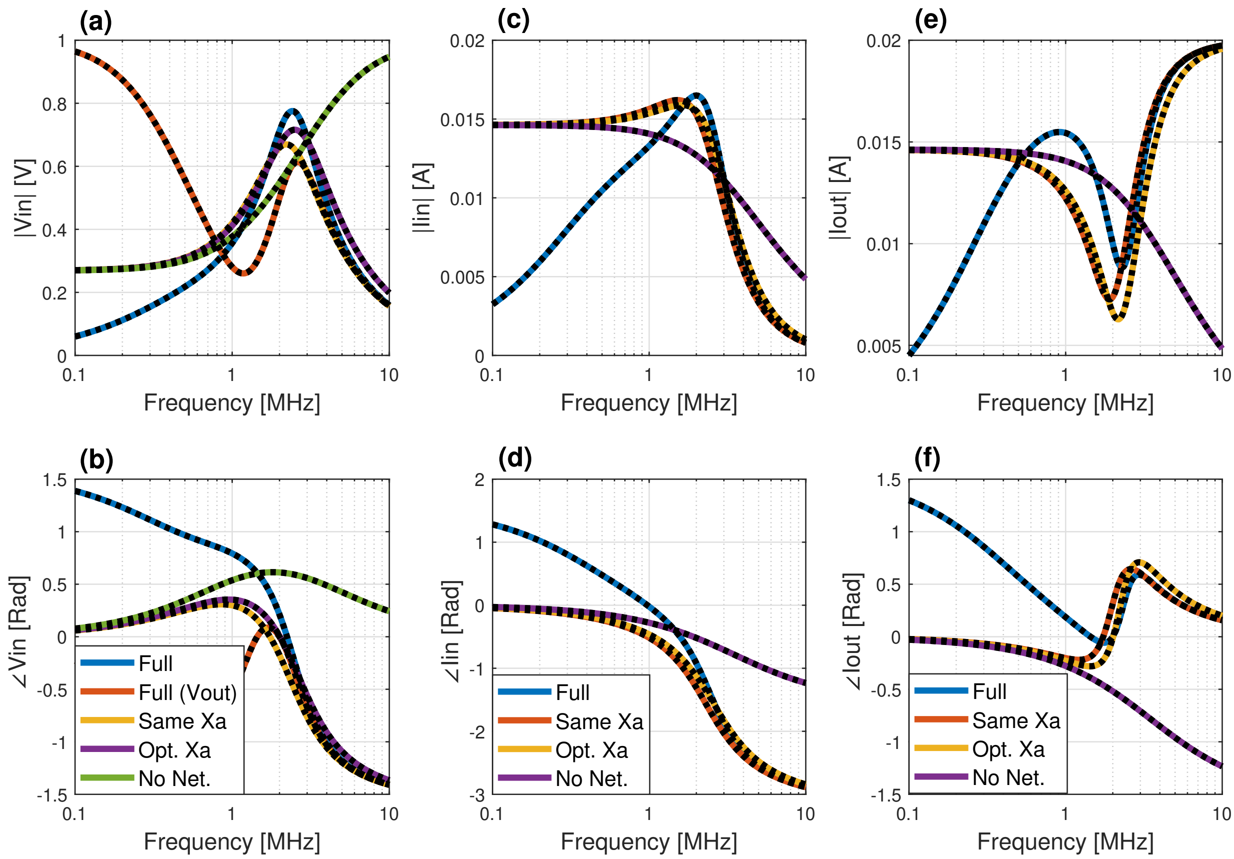

Figure 5.3: Simulations in LTspice are represented by solid, colored lines, while the simulation done in Matlab are the black dashed lines plotted on top. (a) and (b) represent the module and phase of the voltage input of the EMAT respectively. (c) and (d) the current input of the EMAT, and finally (e) and (f) represent the amplitude and phase of the current output by the source.

currents obtained with LTspice. Results show that they match, which confirms the validity of the Matlab model. The latter is used hereinafter for subsequent analysis. To compare the matching network's effectiveness, the absolute value of the voltage across the EMAT is used, as its behavior is the same as the power over the transducer.

A new simulation was performed using the values for the frequency of 2 MHz, this time including both transducers, namely, RPDR#2's EMAT and HWS2225. Both parallel and series one-element networks were evaluated. The results are shown in Fig. 5.4 (a) for the RPDR#2's EMAT and Fig. 5.4 (b) for the HWS2225. It is possible to see that at this excitation frequency, X_a is more effective than X_b for both transducers. It is worth mentioning that although for some curves the peak voltage does not coincide with the target frequency, these are the best configurations for 2 MHz.

One interesting possibility is to alter the Matlab model so it receives the

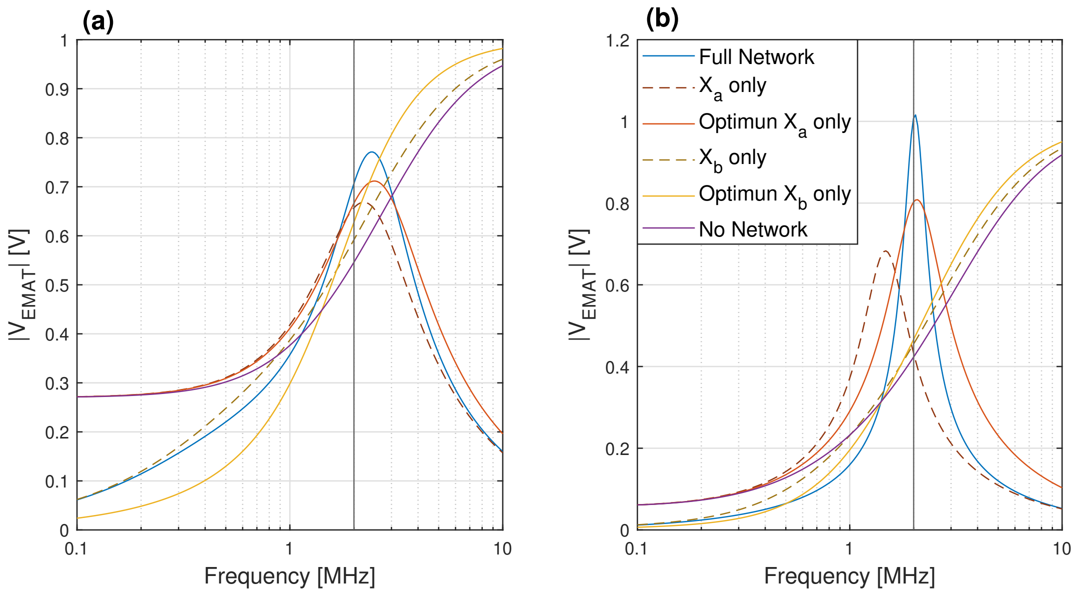

Figure 5.4: Simulations done in the Matlab model for voltage across both EMATs around the intended excitation frequency of 2 MHz indicated by the vertical black line. (a) for RPDR#2's EMAT and (b) for HWS2225. In both graphs, the blue line represents the results for the full network, the orange dashed line for using only X_a with the same value as the full network, the orange solid line for only X_a with optimum value, the yellow dashed line for X_b with the same value as the full network, the yellow line for only X_b with optimum value and finally the purple line represents the results for the circuit with no matching network.

values of R_0 and L_0, or X_0 as a function of the frequency (in an array format). Therefore, more accurate results could be obtained since the EMAT's impedance varies with frequency, as shown in Chapter 4. Fig. 5.5 compares simulations performed with the same load impedance for every frequency, namely the values presented in table 4.1 and simulations performed by inputting the measured impedance results obtained with the impedance analyzer into the model. The darker dashed lines represent the results for the former, the 2 MHz equivalent, and, brighter solid lines represent the results for the latter, the one with corrected impedance for every frequency. Note that, both methods yield the same results at 2 MHz, as expected, but there are significant differences in other frequencies, highlighting the importance of correcting the EMAT impedance for every frequency.

Furthermore, it is also possible to vary the matching network's values over frequency. This can be done by changing the inputs of Eqs. (3-4) and (3-5) to depend on frequency as numerical arrays. Fig. 5.6 shows the complete bandwidth for each transistor, where the networks values are calculated for each frequency. Fig. 5.6 (a) and (c) indicate the transducer's response as a

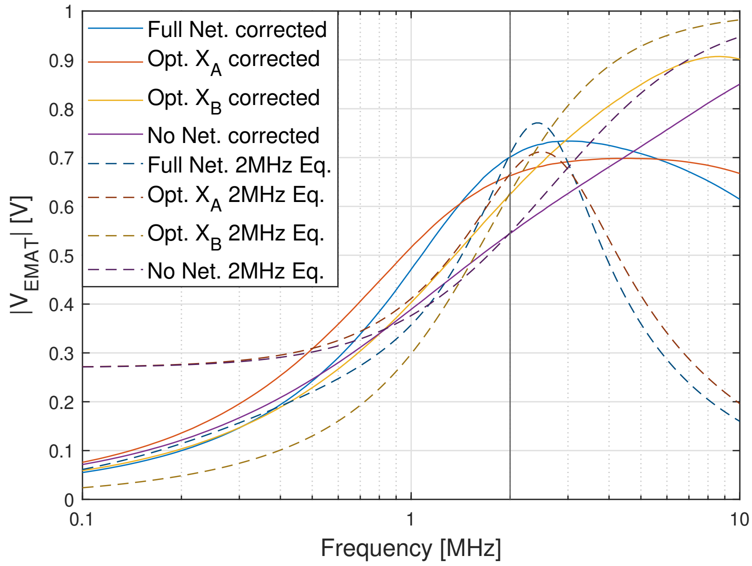

Figure 5.5: Simulation of voltage across RPDR#2's EMAT considering the frequency dependence nature of the EMAT impedance. Blue lines stand for full network, orange lines stand for optimum one-parallel-element (X_a) network, yellow lines stand for optimum one-series-element (X_b) network, and purple lines stand for no matching network. Darker dashed lines were done using the same load impedance for every frequency, namely, the equivalent elements around 2 MHz presented in table 4.1 used in previous simulations. Brighter solid lines were simulated with direct input from the impedance analyzer, using the correct EMAT's impedance at each frequency.

function of frequency, (a) for the RPDR#2's EMAT and (c) for the EMAT model HWS2225. In both plots, it is possible to see that the natural response, without any matching network (purple line), is always lower than any other network, and the full network (blue line) provides the best voltage amplitude over the transducer, causing resonance in the steady-state sinusoidal regime which can result in a higher voltage than the normalized source. Both the optimal one-parallel-element (orange line) and the optimal one-series-element (yellow line) fall between the full network and no network as expected. Also, HWS2225 generally has a higher response and is more efficient than RPDR's EMAT. This is in accordance with the measurements in Chapter 4, where the HWS2225 has a lower resistance, and a higher reactance to resistance ratio, or impedance phase. Intuitively, this means that less energy is wasted on the transducer's internal resistance. In both cases, there is a frequency where the internal resistance is greater than the source's output impedance (50 Ω). At this point, the solution for the full network in Fig. 3.1(b) is no longer possible being required the circuit in Fig. 3.1(a). This circuit was not explored here, meaning that at this frequency the curve for the full network (blue line) is no longer plotted. Because of its higher resistance, this point arrives at lower frequency for the RPDR's EMAT, namely 4.84 MHz compared to 8.12 MHz, for the HWS2225.

Fig. 5.6 (b) and (d) represent the matching networks values for the simulations in (a) and (c) respectively. Dashed lines represent the reactance values of components X_a and X_b, solid lines represent these values conversion to capacitances. The former has its vertical axis on the right and the latter on the left. The point where the network in Fig. 3.1(b) is no longer possible is also reflected in Fig. 5.6 (b) and (d), where the reactance of elements of the full network (blue dashed lines) are discontinuous at 4.84 MHz or 8.12 MHz. At this point, the full network curves in Fig. 5.6 in (a) and (c) intercept the optimum one-series-element X_b.

Another point of interest is where the full network's results meet the optimum one-parallel-element's (X_a) result in Fig. 3.1(a) and (c). This, intuitively, occurs when the full network's X_b is zero. This means that, below this frequency, the full network requires an inductor, a fact also indicated in the darker blue lines of graphs (b) and (d). This point is at 653 and 750 kHz for RPDR's EMAT and HWS2225 respectively.

This complete simulation can be used to determine, for each transducer, the excitation frequency that provides the best resulting amplitude. It is worth mentioning that, the impedance matching network is intended to be used, with other types of EMATs, at lower frequencies, in the future. This was not explored in this work due to the RPDR pulser-receiver module bandwidth from 2 MHz to 6 MHz. Considering a specific intended operating frequency, this simulation also informs the decision of the best configuration and values of matching network needed.

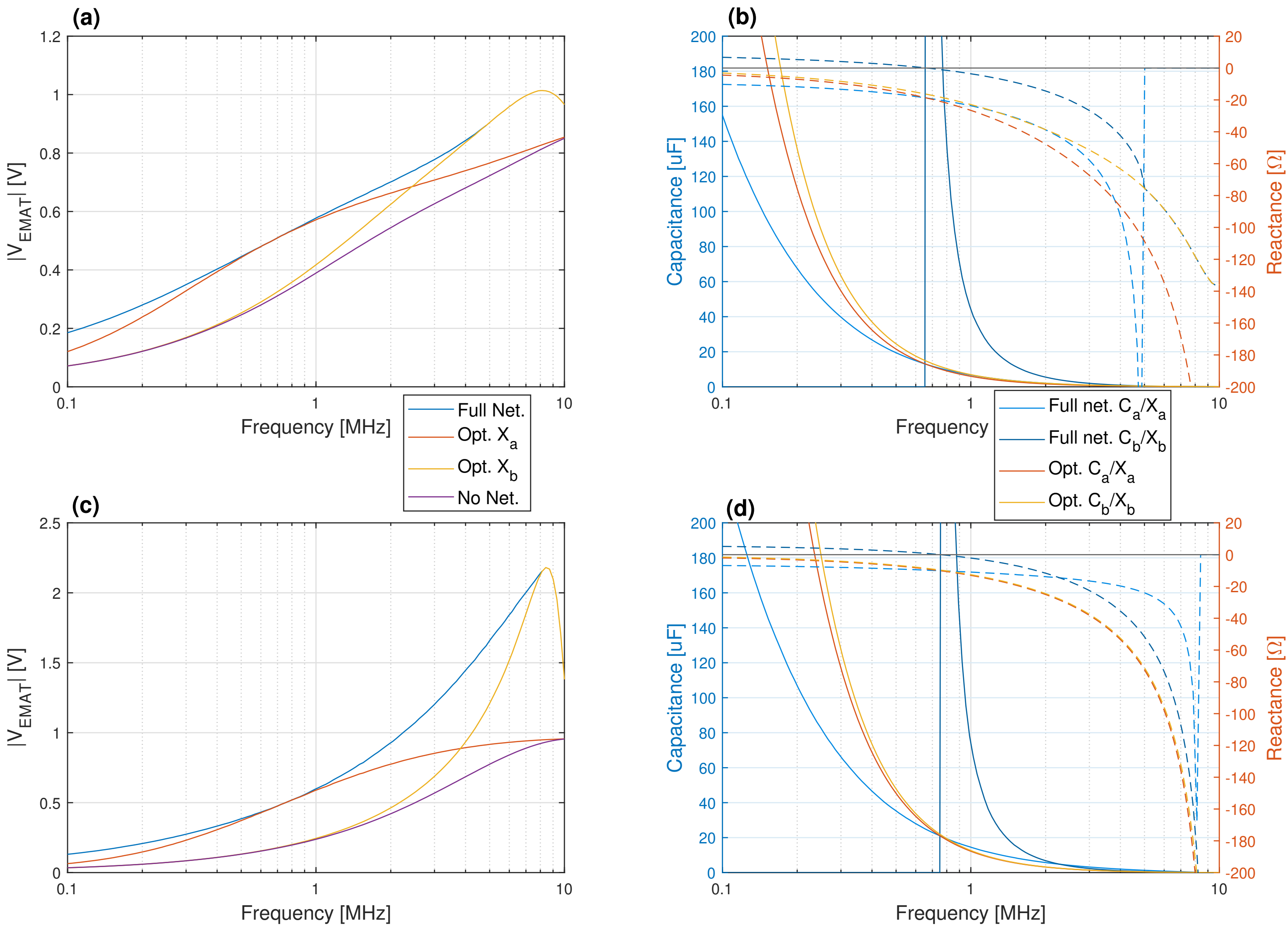

Figure 5.6: Simulations made with the correct impedance, and best matching network's values for each frequency. (a) Voltage across RPDR#2's EMAT. (b) Values of the components of the matching networks for the simulation of the RPDR#2's EMAT. (c) Voltage across HWS2225's EMAT. (d) Values of the components of the matching networks for the simulation of the HWS2225's EMAT. For (a) and (c): the blue lines represents the full L-matching network, orange lines the optimum one-parallel-element (X_a) network, yellow lines the optimum one-series-element (X_b) network, and purple lines for no matching network. For (b) and (d) dashed lines represent the reactance values of the network's elements used in the simulation to the left, solid lines represent the respective capacitance at each given frequency. Blue lines indicate the values used in the full network simulation, lighter shades for elements in the X_a position and darker shades for elements in the X_b position, orange lines for optimum one-parallel-element (X_a) network, yellow lines for optimum one-series-element (X_b) network.

6
Matching networks built and experimental setup

This chapter is divided into two sections. The first one describes the networks that are fabricated, namely a manual network, a preliminary automatic network, and a final automatic network. The second section explores the experimental setups that use these networks. The equipment and configurations used are described and schematics are presented for a through transmission setup, a pulse-echo setup, and a second pulse-echo setup that uses a hardware peak detector.

6.1
Matching networks built

As explored in Chapters 3 and 5, a simplified one-element network can provide a large part of the efficiency gain that can be achieved using the full network. Taking this into account, with other factors such as ease of construction, and the intended excitation frequency range, a simplified one-parallel-element (X_a) network was chosen to be experimentally built and tested, using only capacitors in the X_a position. As seen in the previous chapters, only capacitors are needed for the one-element matching networks, and compared to inductors, they are less expensive and readily available. In order to change the capacitance value of the X_a element, a bank of capacitors in parallel was used with approximately binary weights. Each capacitor in the bank was connected or disconnected to node A in Fig. 5.1(b), so that the equivalent element X_a has a value equal to the sum of all the capacitors in the bank that are connected. If the network was intended to be used at higher excitation frequencies, a one-series-element (X_b) configuration would provide better results.

It is worth mentioning that, due to the EMAT's low efficiency, a lot of energy is put into the system by the source (pulser). The pulser used in all the experiments was a RPDR-100 compact EMAT pulser-receiver OEM module from Ritec, which is capable of providing up to 1000 V into a transducer. Considering the explored EMAT's impedance, the peak power is very high, even if the average power is much lower considering the burst operation. This means that the components used to build any matching network should be dimensioned to withstand the system's power.

6.1.1
Manual network

The first network built uses manual switches to make the connection between the eight capacitors in its bank and node A in Fig. 5.1. In this case, the switches were C&K model 7101, chosen for their low internal resistance. Film capacitors with a voltage rating of 1600 V were used [35]. To further divide the voltage across each capacitor, they were associated in series, meaning that for each of the nominal values in the capacitor bank, two components with double the capacitance were used, each one withstanding half the voltage. The nominal or equivalent capacitor values in the manual network's bank are 0.11 nF, 0.25 nF, 0.5 nF, 1 nF, 1.875 nF, 3.75 nF, 7.5 nF, and 14.0 nF. Besides the capacitor bank, the network also has a 40db attenuator, which is used to monitor the excitation signal with an oscilloscope. The attenuator was constructed with a 2475 Ω 5W resistor from the input and another 49.9 Ω pulldown resistor. Fig. 6.1 presents the circuit schematic of the manual network. Fig. 6.2 (a) and (b) show photographs of the front and back sides of the constructed manual network respectively.

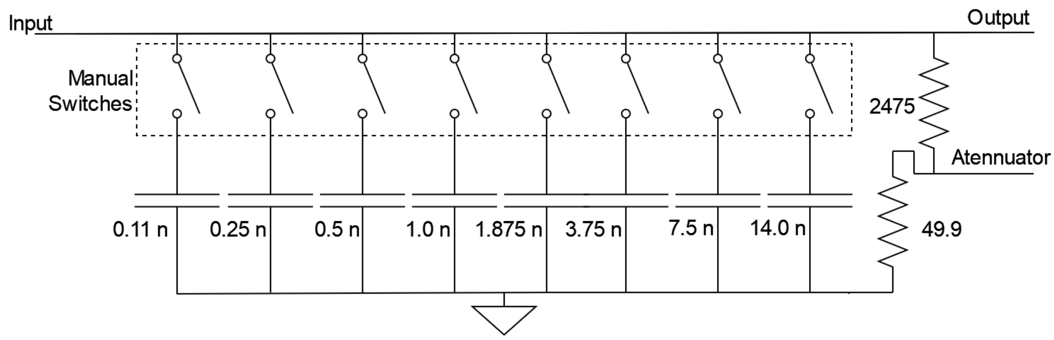

Figure 6.1: Circuit schematic of the manual one-parallel-element matching network.

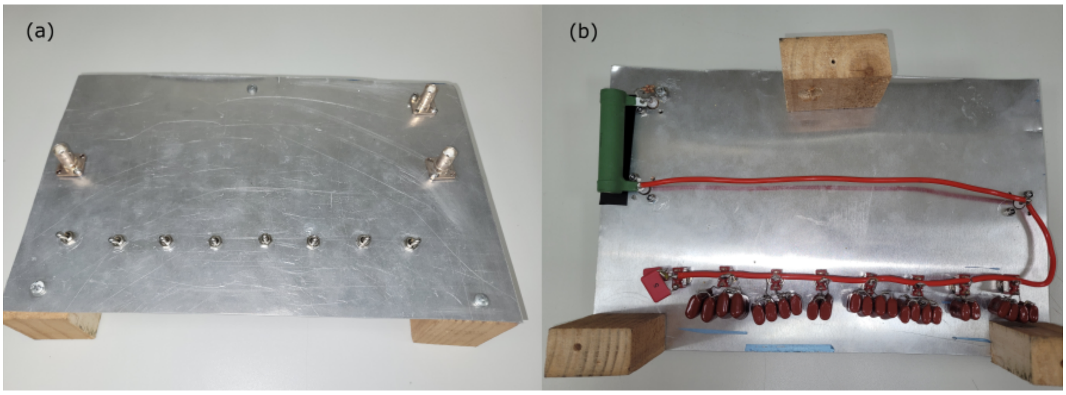

Figure 6.2: Photograph of the manual one-parallel-element matching network. (a) front side, (b) back side.

6.1.2
Preliminary Automatic network

A preliminary automatic network was constructed using a bank of only five capacitors, which are switched by Metaltex AX1RC-5v relays, chosen because they were readily available and rated for 10 A at 250 VAC [36]. The relays are operated by an ESP32 microcontroller [37], which met all the requirements for the automatic network, namely the number of digital ports and WiFi communication. The digital ports of the microcontroller, whose output is 3.3 V, could not reliably actuate the 5 V relays, and the microcontroller was not capable of supplying enough current to control many relays. Therefore, a simple circuit with a transducer was used for each relay to be activated. The control part of the circuit was constructed in a breadboard, the relays, capacitors, and attenuator were simply soldered using speaker wire, terminating in female BNC connectors. The values of the capacitors in the bank are 0.5 nF, 1 nF, 1.875 nF, 3.75 nF, and 7.5 nF. This network also possesses a similar attenuator as used in the manual network. A photograph of the built preliminary automatic network can be seen in Fig. 6.3.

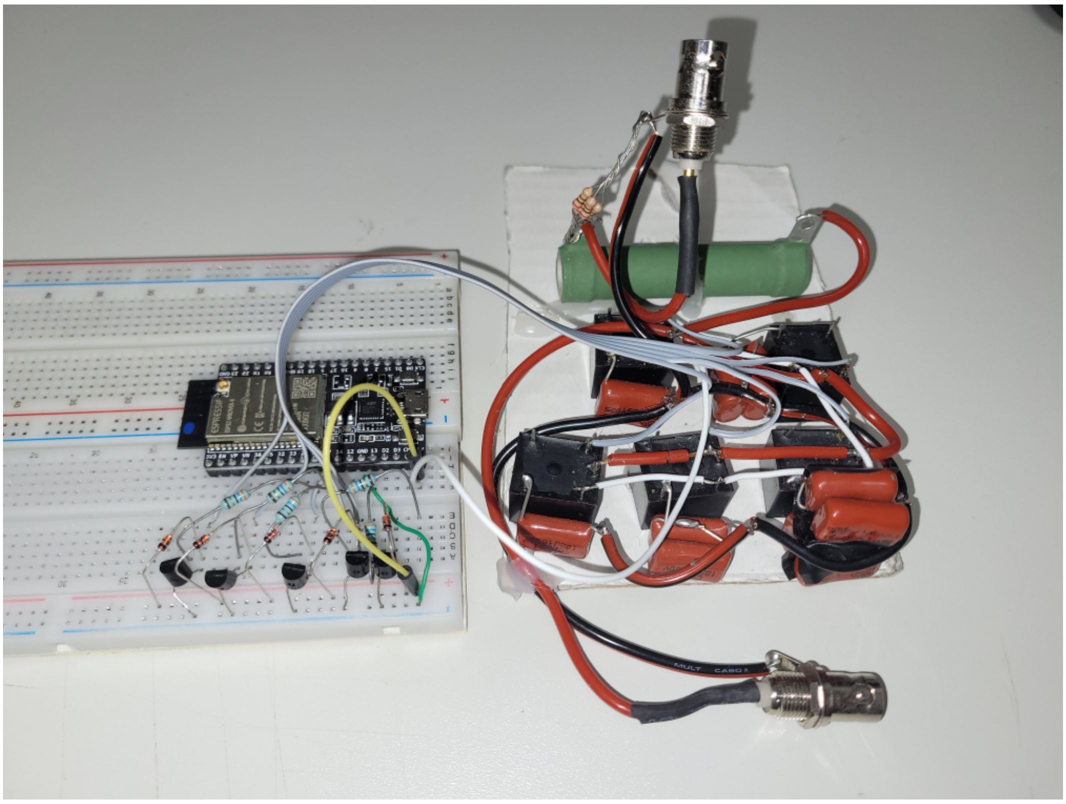

Figure 6.3: Photograph of the preliminary one-parallel-element matching network.

6.1.3 Final Automatic network

Next, a more refined version of the automatic network was built in a custom-made printed circuit board (PCB), using the same relays, microcontroller, and attenuator. This network has a bank of eighth capacitors whose values are: 0.11 nF, 0.235 nF, 0.5 nF, 1 nF, 1.95 nF, 3.4 nF, 6.0 nF and 11.0 nF. They are not the exact same values as the manual one, but cover the same range. The schematic of the circuit is shown in Fig. 6.4. The board design can be seen in Fig. 6.5(a), and a photograph of the finished board is shown in Fig. 6.5(b).

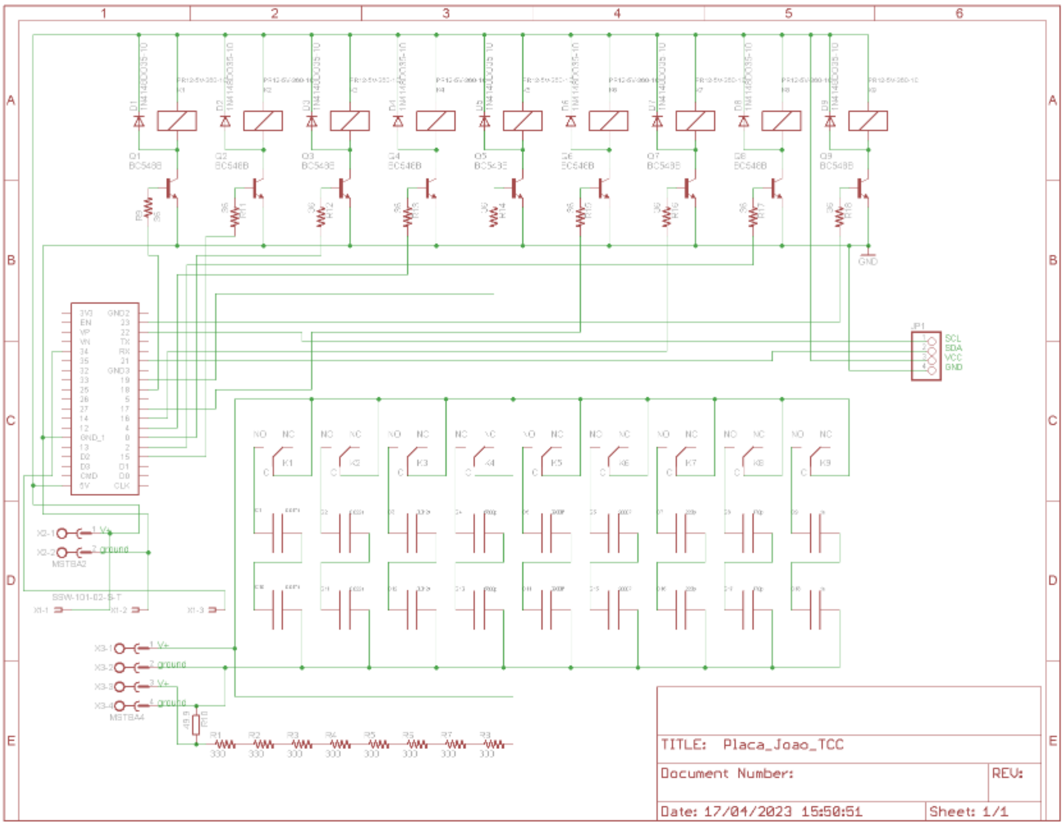

Figure 6.4: Schematic for the automatic one-parallel-element matching network board made in Eagle.

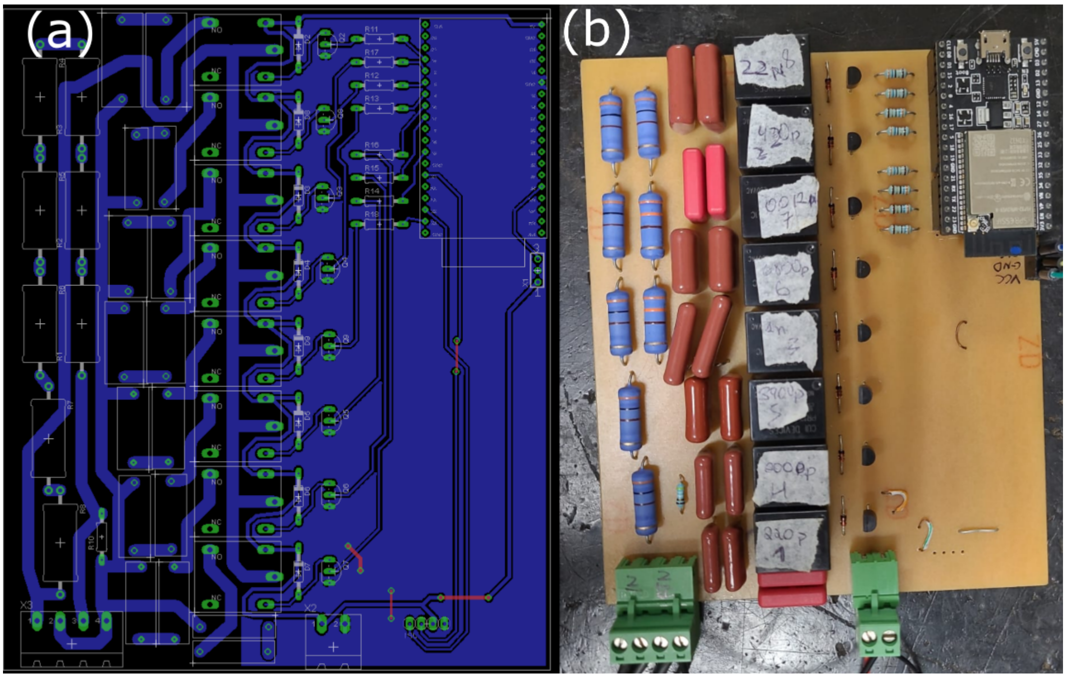

Figure 6.5: Automatic one-parallel-element matching network board. (a) PCB design made on Eagle. (b) photograph of the finished board with all components soldered.

6.2 EMAT based ultrasonic transmission experimental setup

Once the matching networks have been addressed, the whole experimental setup is reported in this section. It is worth mentioning that the tests described in this section were performed with three excitation frequencies: 2, 3, and 4 MHz. Lower frequencies were not used due to the 2-6 MHz bandwidth of the RPDR modules.

6.2.1 Through transmission with preliminary network

The first tests used both the RPDR's EMATs in a through transmission setup. This means that both transducers were positioned on opposite ends of the 12 mm steel block, so that one EMAT operated as a transmitter, generating ultrasound waves that propagate across the medium, and the other EMAT receives the ultrasound waves and converts them to electrical signals. These tests were performed using both the Manual network and the Preliminary Automatic network. In the former, only the five capacitors in the capacitor bank that share the same value as the preliminary automatic one were used. A simplified schematic of this experimental setup, which highlights the matching circuit exploited in the previous chapters, is shown in Fig. 6.6. A detailed schematic containing all the connections between the different equipment used on the experimental setup can be seen in Fig. 6.7.

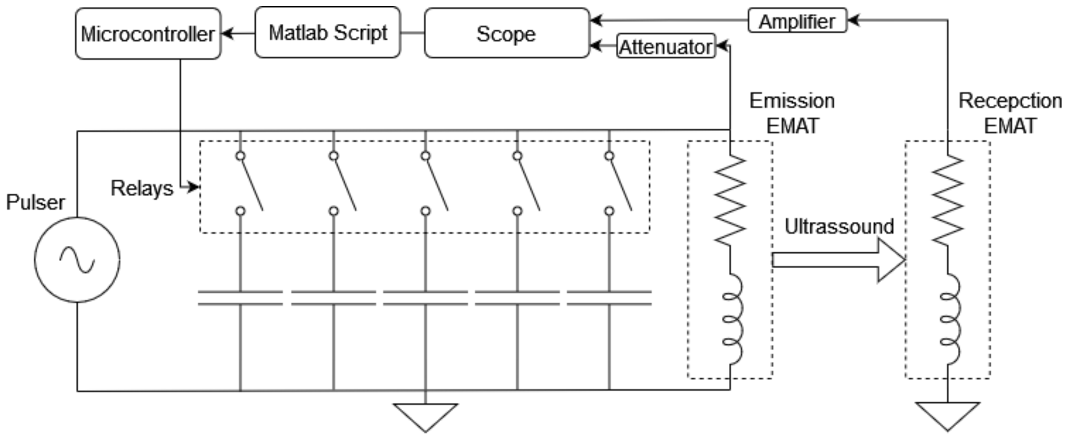

Figure 6.6: A simplified schematic of the through transmission experimental setup, which highlights the circuit composed of the pulser, matching networks, and load, in this case, the EMAT. The preliminary one-element matching network consists of five capacitors in parallel, each of which is added or removed by a relay. The transmitter voltage over the EMAT passes through an attenuator prior to being connected to an oscilloscope. The receiver EMAT captures the propagated ultrasonic wave across a steel medium. The received signal is then amplified prior to being sent to an oscilloscope. A Matlab script is used to request the measurements from the scope and request the relay changes from the microcontroller via WiFi, which in turn activates the relays.

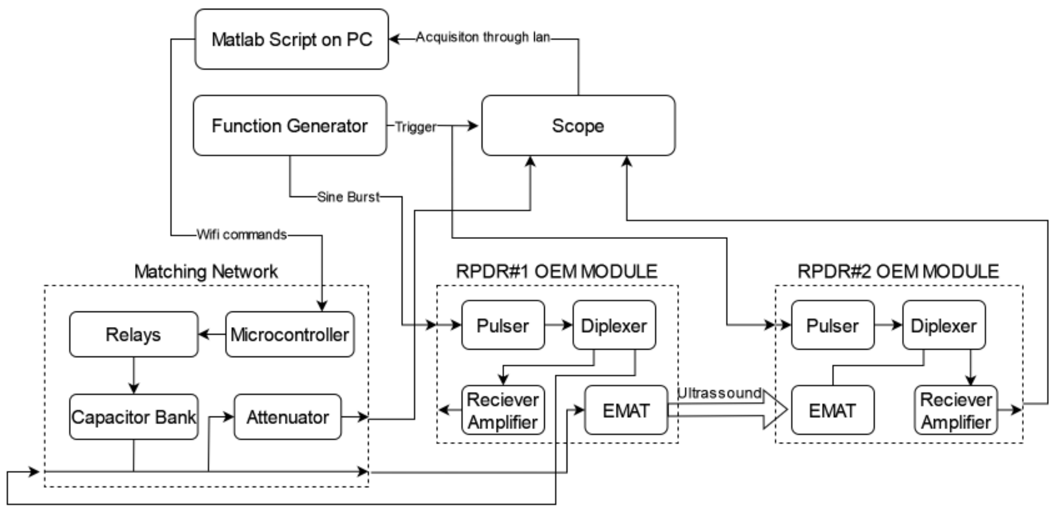

Figure 6.7: Schematic of the through transmission experimental setup, containing all the connections between the different equipment used in the experimental bench.

A full sweep of all the possible network values was executed, saving the waveforms of the attenuator and receiver amplifier for each configuration. A Matlab script running on a Linux computer was used to control the sweep. This script can send commands to the microcontroller via WiFi and request the network to change to any value in the capacitor bank. The scope's data is also acquired via LAN by the Matlab script.The data can then be saved and later analyzed and interpreted. The function generator, set to an internal trigger, outputs a 5-cycle sine tone-burst into the transmission RPDR's input. This signal is amplified by the RPDR#1's pulser and it passes through the matching network before arriving at the RPDR#1's EMAT. At this point, the EMAT generates an ultrasonic wave that propagates through the steel block and is captured by the RPDR#2's EMAT. The receiving transducer's resulting signal passes through the RPDR#2's receiver, which consists mainly of an 80 dB amplifier. The scope then measures this output of the RPDR#2's receiver, and also the signal at the matching network's attenuator. That is, the scope monitors the signal that goes into the transmission EMAT and out of the receiver EMAT. This process starts with the function generator and can occur many times, for each time the Matlab script requests a specific configuration and acquires the scope's values. For this test, the Scope was set to average 32 acquisitions. The last connection worth mentioning is the trigger signal from the function generator that is used by the scope and also in the RPDR#2's input, as it needs a signal input to 'wake-up' and power its components, mainly the receiver amplifier. Both RPDR modules also have several DC power connections not represented in the schematics. For the RPDR#2 module, the high voltage input was disconnected, which means it operates in the receiver mode.

6.2.2
Pulse-Echo with final network

The tests in this subsection were performed with the Automatic network constructed in the PCB, and with the manual network. The 'pulse-echo' setup uses only one transducer, which acts as transmitter and receiver. Two tests with both EMAT models were performed, namely, RPDR#2's EMAT, and the HWS2225 transducer. Apart from these main differences, the rest of the setup is similar to the one used for the through transmission. Fig. 6.8 and Fig. 6.9 show the schematics of this setup with the differences between the through-transmission setup highlighted in red. It is worth mentioning that the same RPDR-100 pulser-receiver module was used for measures with both transducers. Also, due to the HWS2225's higher efficiency, the RPDR's receiver amplifier was set to a 58 dB gain for the tests involving this transducer. All tests with the RPDR's EMATs were done with the usual 80 dB gain.

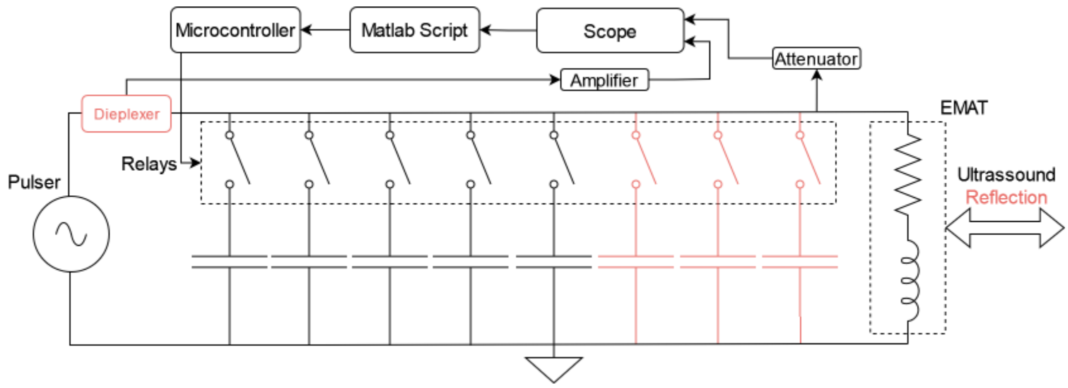

Figure 6.8: A simplified schematic of the pulse-echo experimental setup, which highlights the circuit composed of the pulser, matching networks, and load, in this case, the EMAT. The differences from Fig. 6.6 are highlighted in red. They are the addition of three more capacitors to the network, and the diplexer whose output goes to the amplifier. The ultrasound signal captured here is the reflection from the boundary of the steel block. It is worth mentioning that the elements, mainly the reception EMAT, from Fig. 6.6 that are not present here are not highlighted but simply absent.

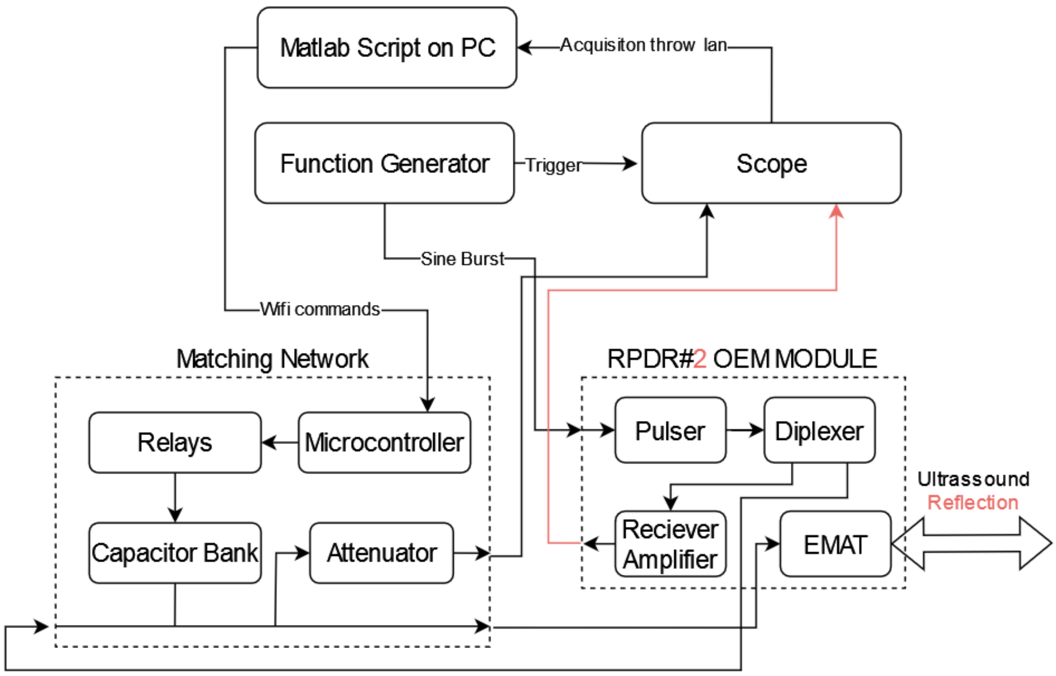

Figure 6.9: Pulse-echo experimental setup schematic. The differences from the schematic in Fig. 6.6 are highlighted in red. The elements from Fig. 6.6 that are not present here are not highlighted but simply absent. The EMAT is shown inside the RPDR module, but there were tests, with the external HWS2225 transducer.

6.2.3
Pulse-echo with final network and hardware peak detector

In order to speed up the process and make a fully automated network, a peak detector inside the matching network that feeds information directly to the microcontroller was used. Therefore, the oscilloscope and Matlab script are no longer needed. The oscilloscope was used in this experiment exclusively to save the data for post-analysis. As per the introduction section, the main goal of this thesis is to build a, convenient to use, matching network that is placed between the pulser and the transducer and does not require any other connections in order to provide the optimal matching configuration.

The peak detector is connected to the output of the attenuator and its value is read by an external analog-to-digital converter (ADC) model ADS1015 [38], as the microcontroller's internal analog readers were experimentally deemed inconsistent for this application and the ADS1015 was readily available. The topology of the peak detector is shown in Fig. 6.10, and was based on [39]. The circuit works by storing its highest input value in the capacitor (C1). A diode (D1) is used to remove the negative parts of the input. The input signal then passes through an operational amplifier (opamp, U1) which acts mainly as a buffer, and then, through another diode (D2), the capacitor is charged. This diode guarantees the capacitor does not discharge when the signal is negative, since it becomes reversed-biased. The second opamp (U2) is configured as a voltage follower, it provides the output of the circuit which is the same as the voltage across the capacitor. To discharge the capacitor, a resistor (R4) is used in parallel to it. This resistor's value regulates the rate of discharge. In this circuit, a NPN transistor was used in series with R4, so that the signal label 'Control' can determine whether and when the peak detector is discharged. It is also worth mentioning that a third diode (D3) is used in the negative feedback for U1, so that the voltage drop across it can match the voltage drop across D2, therefore not affecting the output.

The timing of the peak detector's reading needs to be considered. In this case, the sine tone-burst, or bang can last from 1.25 to 5 μs, and it causes interference. If the peak detector's output was built to discharge over time, the ADC reading of it would need to be right after the sine tone-burst when this value is maximum. The ADC's reading is requested by the microcontroller via I2C protocol [40], and takes at least 6 ms. This is not fast enough to guarantee a reading at the right time simply by polling the ADS. Therefore, the peak detector is not discharged over time, and a transducer is used so that the microcontroller can choose when it is discharged, doing so quickly, before the next tone-burst excitation signal is triggered. To be able to do this,

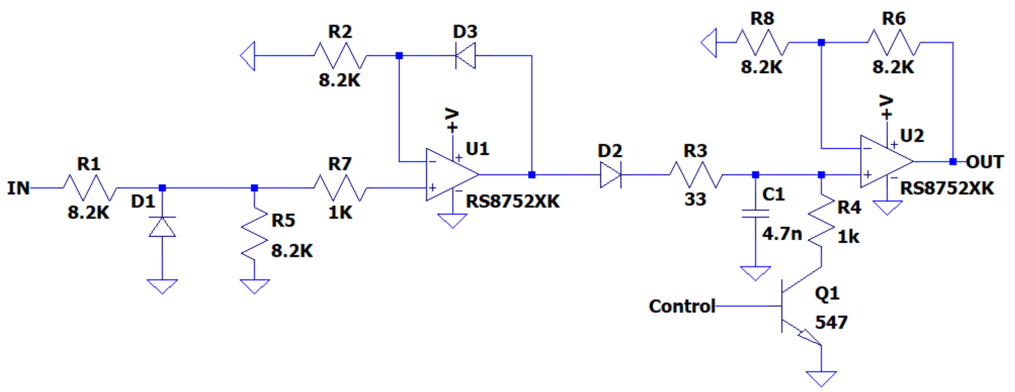

Figure 6.10: Peak detector circuit based on the 'Improved Peak Detector' in [39]. In this setup, the input 'IN' node connects to the matching network's attenuator, the output 'OUT' connects to the ADC, and the 'CONTROL' node connects to a digital output in the microcontroller.

the microcontroller was programmed with a digital port *interrupt*, using the function generator's trigger rising edge, as a general synchronization signal. It is worth mentioning that a low-pass filter was also used to connect the trigger to the microcontroller's *interrupt* to avoid the bang's interference, which would result in many rising edges in the trigger signal and various subsequent interrupts. To eliminate the connection between the function generator and the microcontroller, it can also be replaced by a comparator activating the microcontroller's interruption by using the peak detector's signal rise. After the *interruption* the microcontroller waits 10 ms to request the ADC's reading. After the reading is saved, the microcontroller discharges the peak detector.

Fig. 6.11 shows the signals for the attenuator's output, which is the peak detector's input, the peak detector's output, and the trigger. Fig. 6.11 (a) and (b) shows these signals at a time scale where the bang's interference can be seen. Fig. 6.11 (c) shows the same signals at a wider time scale, where the discharge of the peak detector can be seen. The bang and its interference, cannot be seen in Fig. 6.11 (c) due to its short duration and the high time between samples in this wider time scale. The detailed schematic of this setup can be seen in Fig. 6.12.

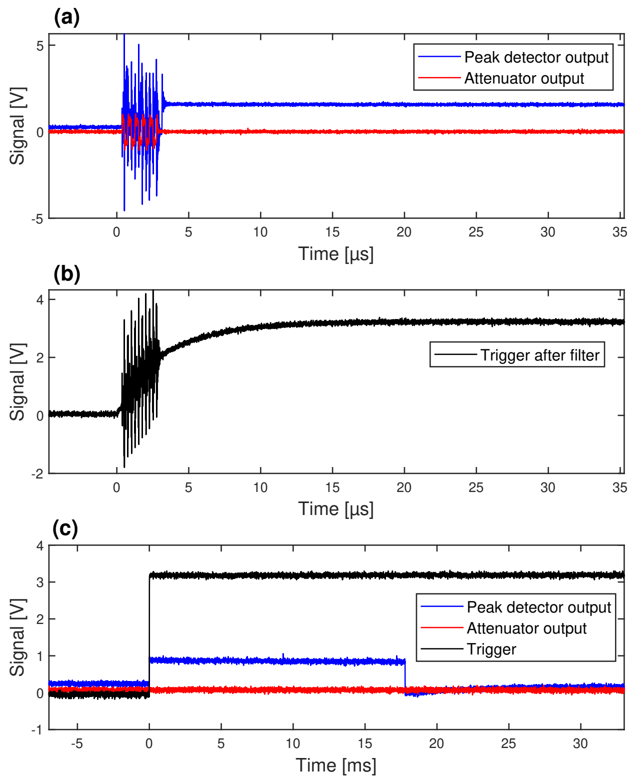

Figure 6.11: Signals measured with an oscilloscope. (a) shows the peak detector's input (attenuator's output) in blue, and its output in red. (b) shows the trigger signal from the function generator after passing throw the low-pass filter in black. Both (a) and (b) have the same time-scale. (c) shows the three signals mentioned previously using the same colors, at a wider time scale.

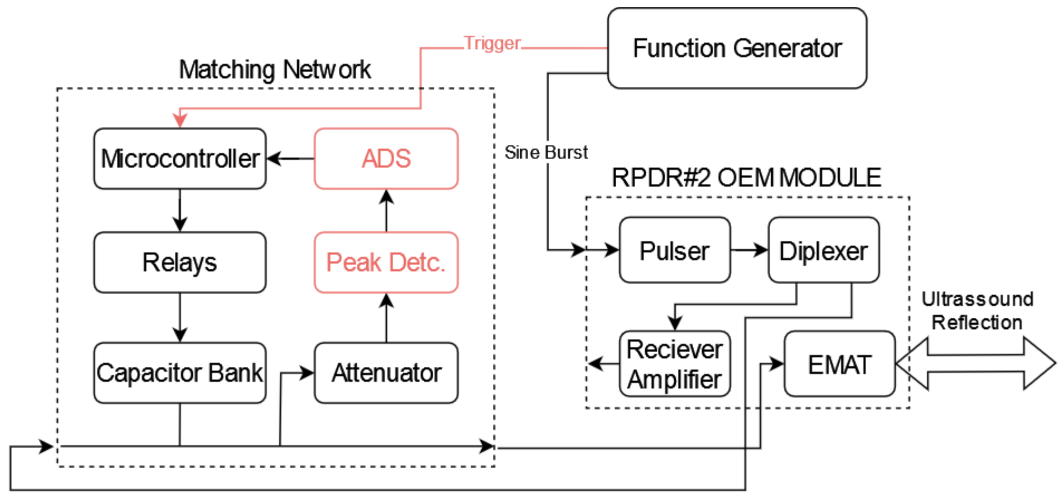

Figure 6.12: Schematic of the experimental setup for the pulse-echo with peak detector. The differences from the schematic in Fig. 6.9 are highlighted in red. The elements from Fig. 6.9 that are not present here are not highlighted but simply absent.

7
Experimental Results

In this chapter, the experimental results for each of the setups explained in Sec. 6.2 are presented. Plots and tables are generated to analyze the effectiveness of the matching networks. Results for different frequencies and transducers are compared.

7.1
Through transmission

Tests were performed as explained in section 6.2.1. Fig. 7.1(a) shows the peak-to-peak amplitude of the transmitted signal as a function of the equivalent capacitance for each capacitor bank configuration. A line is plotted for each of the three operating frequencies, both the manual and preliminary automatic matching networks were used. As expected, each frequency requires a different capacitance value and, consequently, a different configuration of the capacitor bank. The values obtained for the manual and automatic methods are very similar. Fig. 7.1(b) shows the peak-to-peak measurements for the acoustic signal received after it propagates through the steel. Note that, as a consequence of the higher transmitting power, the received signal also is maximum at the same capacitance value as the signal in Fig. 7.1(a). The table 7.1 reports the peak-to-peak voltage over the transmission EMAT for no network and the optimal one-parallel-element network found. It is worth mentioning that, the only capacitance values that differ from the manual and automatic experiments in this table, namely 2.7 and 3.2 nF, have no possible value between them, because of the limited number of values for the matching network's capacitance.

It is also possible to compare the experimental results with the theoretical values, as shown in Fig. 7.1. As can be seen, they show roughly the same behavior, with two main differences. The experimental capacitance for optimal matching is higher than the theoretical one. Also, the higher frequencies have a higher maximum amplitude in the simulations, but the opposite trend is true in the experiments. Several experimental factors can cause those differences. For instance, the source impedance can differ from the assumed 50 Ω, and, as seen before, the load impedance can vary due to many factors. Although measures were taken to eliminate these differences, not all factors can be eliminated,

Table 7.1: Results for the Through transmission. The first column indicates the frequency and the network used for the results in each line. 'Man.' indicates the Manual network, and 'Aut.' the Preliminary automatic network. The second column shows the network's equivalent capacitance which provided the highest signal amplitude. The third column shows the peak-to-peak amplitude of the transmitted signal when the network was set to 0 nF as if there were no network. The fourth column shows the maximum peak-to-peak value when the capacitance in column two was used. The fifth column presents the gain in dB between columns three and four. The sixth and last column shows the time taken to complete the full sweep of network values.

Emission					
	Optimun Capacitance Found [nF]	No network pk-pk [V]	Optimal network pk-pk [V]	Gain [db]	Time for full sweep [s]
2 MHz Man.	3.2	721.6	1195.1	4.382	194.0
3 MHz Man.	1.5	661.4	1150.0	4.804	201.1
4 MHz Man.	0.5	676.5	917.1	2.642	209.0
2 MHz Aut.	2.7	714.0	1364.2	5.623	89.9
3 MHz Aut.	1.5	653.9	1187.6	5.182	90.1
4 MHz Aut.	0.5	638.9	1044.8	4.271	90.5

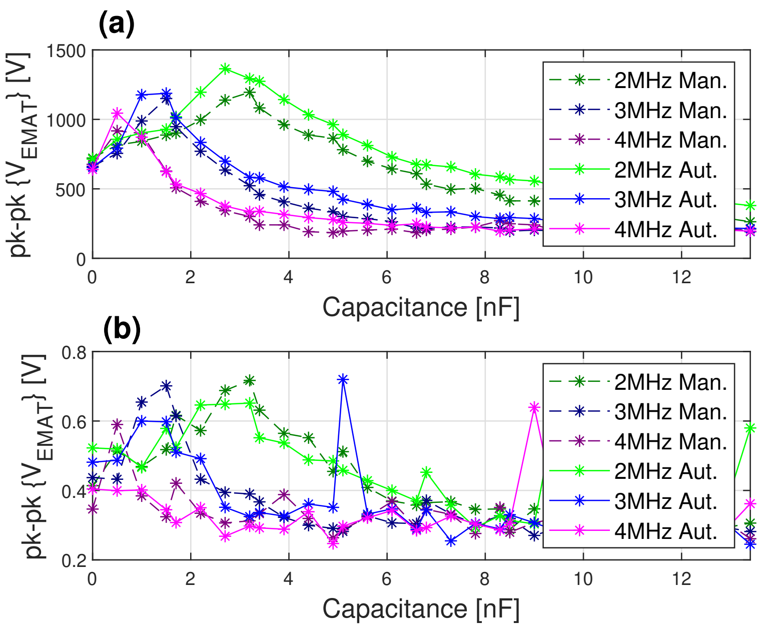

Figure 7.1: Peak-to-peak amplitude at the (a) transmitting EMAT and (b) receiver EMAT as a function of the equivalent capacitance of the capacitor bank, obtained with the manual impedance matching in dashed darker lines, and with the automatic method in solid brighter lines. Three excitation frequencies were evaluated, 2, 3, and 4 MHz, represented by green, blue, and magenta lines, respectively.

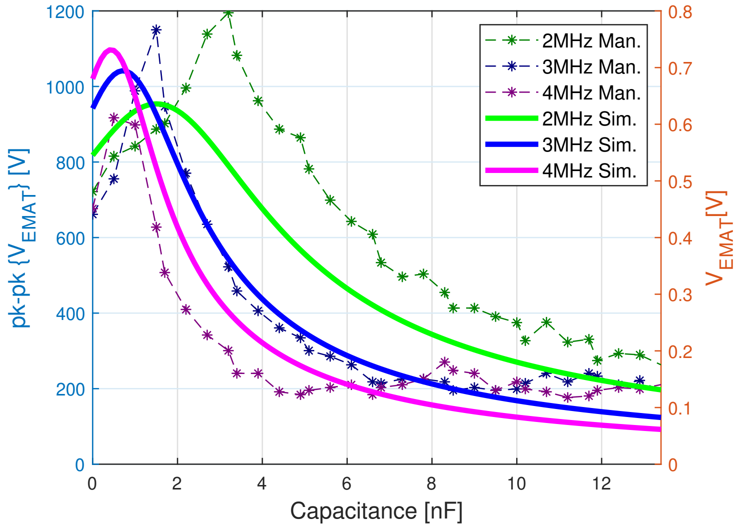

Figure 7.2: Comparison between the experimental and normalized simulation results for each capacitance. Brighter solid lines are the simulation results, whose vertical axis is on the right. The darker dashed lines are for the manual experiment results, whose vertical axis is on the left. Excitation frequencies of 2, 3, and 4 MHz, represented by green, blue, and magenta lines, respectively. The simulation was done with a normalized steady-state sinusoidal wave, however, the pulser used in the experiments provides a much higher voltage sinusoidal burst.

the transducer's temperature, for example, cannot be controlled. Also, as seen in Section 6.2, there are many components connected to the experimental setup, not all of them were considered in the simulations; an example could be the attenuator. Other spurious effects can include the impedance of the cables. In summary, a reasonable agreement was obtained, but some of the deviations are inconclusive. It is worth mentioning that the process of sweeping configurations until reaching the optimum measured results takes into account the whole experimental setup, unlike the theoretical simulations, providing the best practical results. This is befitting with the higher experimental gain than in simulation.

Fig. 7.3 shows the transmitted and received signals for the one-element matching network, set for the best configuration ($C_a = 2.7$ nF) at a 2 MHz excitation frequency (blue line) or without any matching network (red line). Fig. 7.3(a) shows the transmitter EMAT signal, where the 5-cycle sinusoidal excitation pulse, from 0 to around 4 μs, is much higher when the network is used. Fig. 7.3(b) shows the signal at the receiver EMAT, which includes the interference caused by the transmission. This interference is removed from the receiver signal for analysis purposes, as it saturates the scope. The acoustic

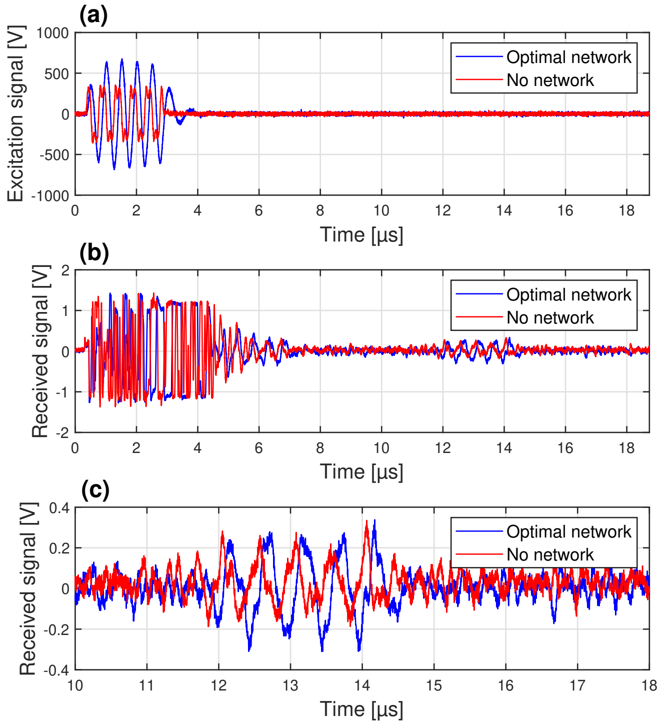

Figure 7.3: Optimal matching network (blue line) effect at 2 MHz on (a) Excitation signal, (b) Received signal, compared to no network used (red line). (c) presents the zoomed-in received signal, discarding the bang's interference and focusing on the received ultrasonic wave between 12 and 14 μs.

received signal appears between 12 and 14 μs, due to the acoustic speed and wave propagating path, it also shows a slight increase when the matching network is used. Fig. 7.3(c) shows the received signal cropped in time with emphasis on the mentioned received signal.

7.2 Pulse-Echo

For pulse-echo tests, the peak-to-peak amplitude of the transmitted signal was analyzed for all possible capacitance values in the matching network and compared with the results without any matching network. The experimental setup was described in Section 6.2.2. This section is divided into two subsections, one for each transducer used.

7.2.1 RPDR's EMAT

Fig. 7.4 shows the peak-to-peak amplitude of the transmitted signal as a function of the equivalent capacitance for each capacitor bank configuration evaluated. Fig. 7.5 shows the comparison between the manual experimental

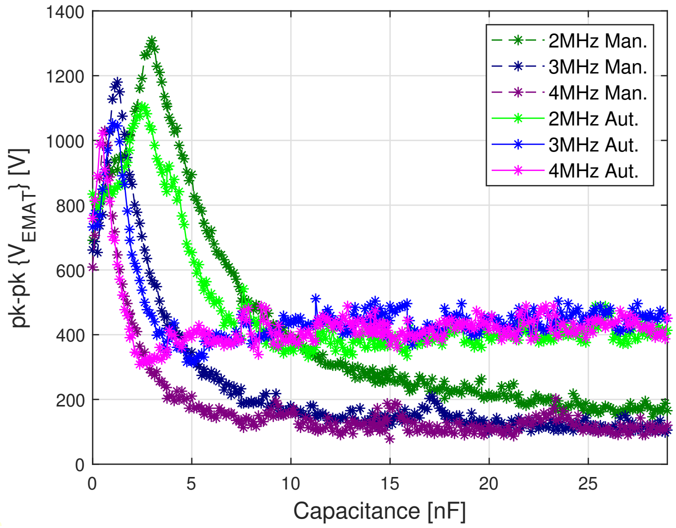

Figure 7.4: Peak-to-peak amplitude at the transmitting EMAT as a function of the resultant capacitance of the capacitor bank. The results obtained with manual impedance matching are in dashed darker lines, and the results obtained with the automatic method are in solid brighter lines. Three excitation frequencies were evaluated, 2, 3, and 4 MHz, represented by green, blue, and magenta lines, respectively.

results and the theoretical values. This comparison follows the same trends as the one in the Through transmission, namely, the experimental capacitance for optimal matching is higher than the theoretical one and the maximum amplitude is higher at higher frequencies in the simulations, the opposite in the experiments. Here, a reasonable agreement was also obtained. Fig. 7.6 shows the waveforms for the no-network and optimum network for the 2 MHz excitation frequency. Finally, for each frequency and matching network used, the values for optimum capacitance, peak-to-peak voltage, gain, and time taken to do the full sweep can be found in Table 7.2. Again, we can see that both manual and automatic methods have similar optimum capacitances for each frequency. Unlike the tests performed with the preliminary automatic network, here the manual results are slightly higher than the automatic ones. The results with the automatic matching network also present more noise, especially with higher capacitances.

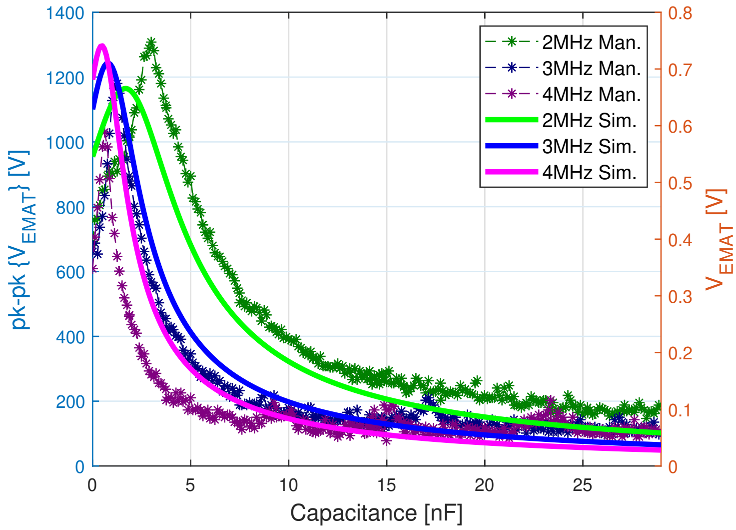

Figure 7.5: Comparison between the experimental and normalized simulation results for each capacitance. Brighter solid lines are the simulation results, whose vertical axis is on the right. The darker dashed lines with star markers are for the manual experiment results, whose vertical axis is on the left. Excitation frequencies of 2, 3, and 4 MHz, represented by green, blue, and magenta lines, respectively.

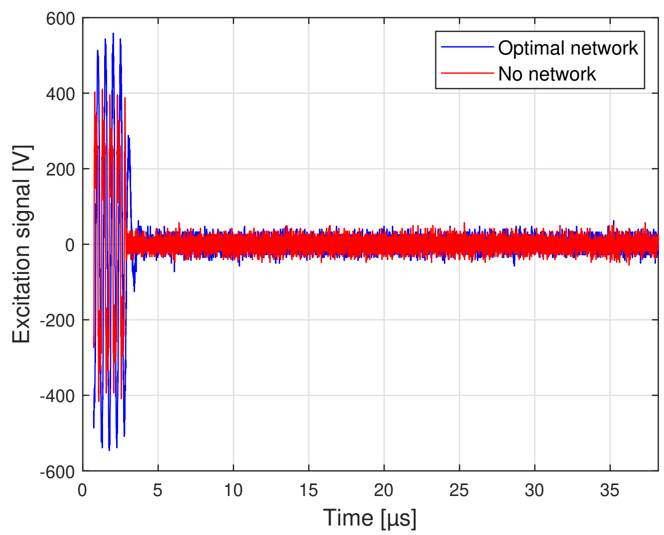

Figure 7.6: Optimal matching network (blue line) effect at 2 MHz on Excitation signal, compared to the signal without any matching network (red line). Resulting voltage at the RPDR's transducer

Table 7.2: Results for the Pulse-Echo using RPDR#2's EMAT

	Optimun Capacitance Found [nF]	No network pk-pk [V]	Optimal network pk-pk [V]	Gain [db]	Time for full sweep [s]
2 MHz Man.	3.06	691.5	1307.9	5.5352	1481.9
3 MHz Man.	1.235	661.4	1180.1	5.0283	1372.7
4 MHz Man.	0.61	608.8	1029.7	4.5647	1241.7
2 MHz Aut.	2.56	834.4	1104.9	2.4386	754.4
3 MHz Aut.	1.0	732.8	1052.3	3.1424	719.3
4 MHz Aut.	0.50	759.1	1022.2	2.5843	718.3

7.2.2 HWS2225

Fig. 7.7 shows the peak-to-peak amplitude of the transmitted signal as a function of the equivalent capacitance for each capacitor bank configuration evaluated. Fig. 7.8 shows a comparison between the experimental results and the theoretical simulations, in this case, the capacitance at which both methods maximum is in agreement. Fig. 7.9 shows the waveforms for the no-network and optimum network at 2 MHz excitation frequency. The significant values can be found in Table 7.3. As the final automatic matching network was already compared to the manual network, the tests in this subsection were done only with the final automatic network. The results are as expected.

Table 7.3: Results for the Pulse-Echo using HWS2225

	Optimun Capacitance Found [nF]	No network pk-pk [V]	Optimal network pk-pk [V]	Gain [db]	Time for full sweep [s]
2 MHz Aut.	3.06	1045.1	1488.1	3.0698	1218.4
3 MHz Aut.	1.235	1002.5	1515.9	3.5917	1229.9
4 MHz Aut.	0.61	852.2	1338.1	3.9191	1231.8

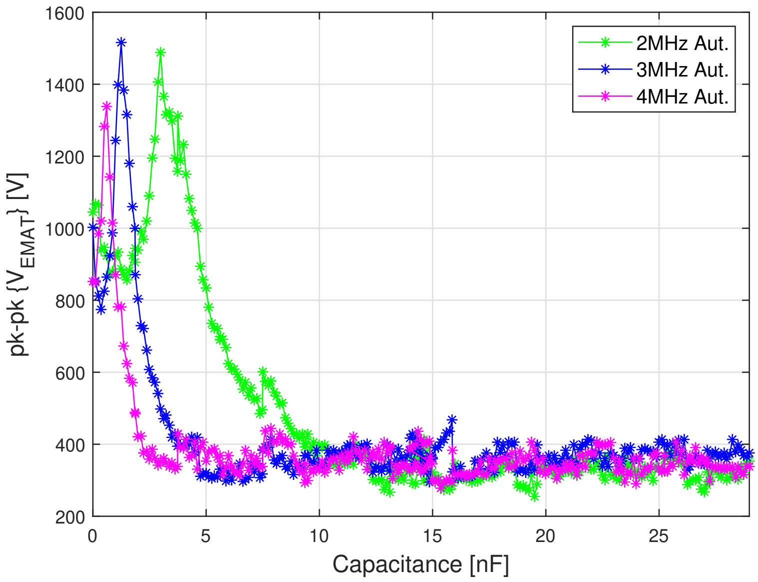

Figure 7.7: Peak-to-peak amplitude at the transmitting EMAT as a function of the resultant capacitance of the capacitor bank obtained with the final automatic matching network. Three excitation frequencies were evaluated, namely, 2, 3, and 4 MHz, represented by green, blue, and magenta lines, respectively.

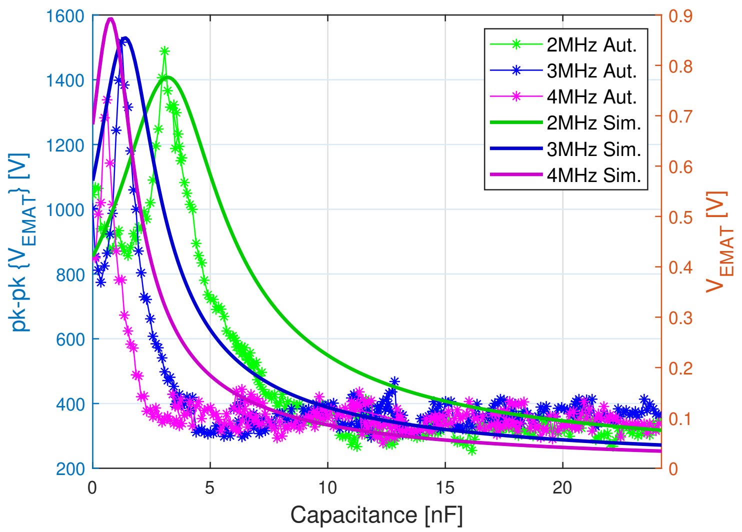

Figure 7.8: Comparison between the experimental and normalized simulation results using the HWS2225 transducer for each capacitance. Solid lines are the simulation results, whose vertical axis is on the right. The lines with star markers are for the automatic experiment results, whose vertical axis is on the left. Excitation frequencies of 2, 3, and 4 MHz, represented by green, blue, and magenta lines, respectively.

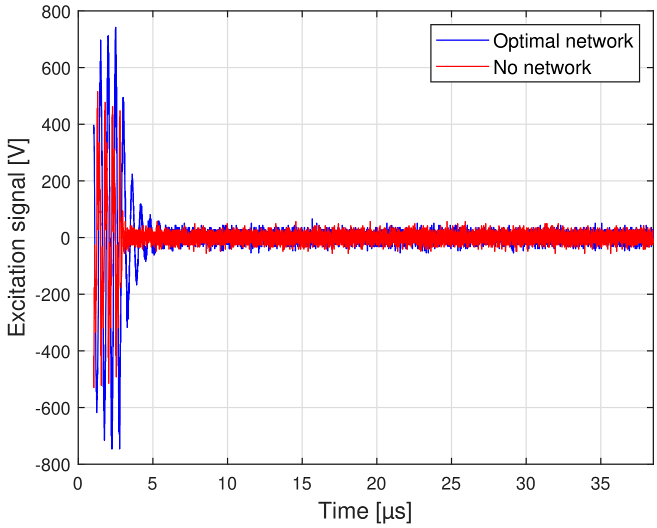

Figure 7.9: Optimal matching network (blue line) effect at 2 MHz on Excitation signal, compared to the signal without any matching network (red line). Resulting voltage at the HWS2225 transducer.

7.3 Pulse-Echo with hardware peak detector

The experimental setup for the tests in pulse-echo with a peak detector is explained in Section 6.2.3. Fig. 7.10 shows the peak-to-peak amplitude of the transmitted signal as a function of the equivalent capacitance for each capacitor bank configuration evaluated. Unlike previous sections, these values were not generated from a waveform in Matlab captured by the oscilloscope, they were captured by the ADS from the peak detector, and saved by the microcontroller. For each frequency, the peak-to-peak voltage with no network, the highest voltage value found, as well as its corresponding capacitance and gain can be found in Table 7.4. The table is divided for each of the two transducers used. It is worth mentioning that the measurements were made 4 times and averaged. With one exception, the four measures for each configuration were consistent in choosing the optimal capacitance value. This exception is the 2 MHz measurement using the HWS2225, where, due to the transducer's higher efficiency, the peak detector was saturated. Because of this, the optimum value of the capacitance varied considerably between sweeps. To solve this, the function generator's output was lowered from the standard 10 V to 8.3 V. This measurement with lower power yielded consistent results and can be seen in Fig. 7.10(b), in the darker green line, labeled as '2MHz LP'. To solve this problem within the network, it is possible to build a second variable attenuator, operated by the microcontroller. It is worth remembering that, for the automatic network, the absolute values are not necessary, only the relative

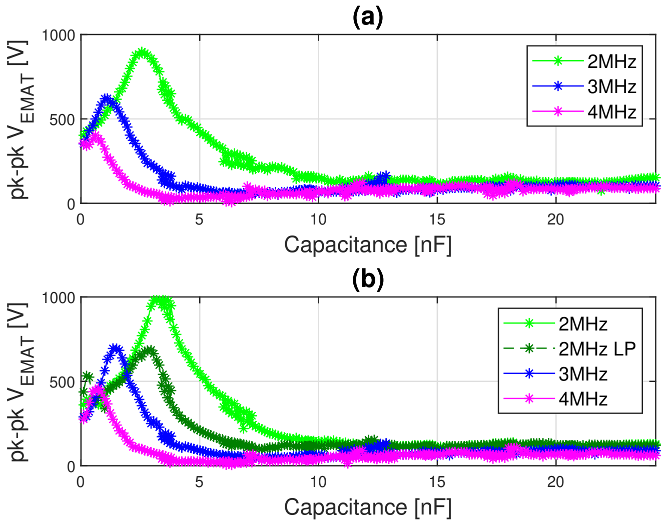

Figure 7.10: Peak-to-peak voltage, measured by the hardware peak detector across (a) RPDR#2's transducer, (b) HWS2225. Three excitation frequencies were evaluated, 2, 3, and 4 MHz, represented by green, blue, and magenta lines, respectively. The darker green line in the bottom graph labeled '2MHz LP' was obtained with lower power to avoid saturation in the peak detector, the normal 10 V excitation from the function generator was switched to 8.3 V just for this measure.

amplitudes between configurations are needed so that the best capacitance can be determined.

The time taken to perform the full sweep depends only on the number of measurements, the average chosen, and the trigger interval set on the function generator, in this case, the values were 256, 4, and 200 ms, respectively. This yields the full sweep time of ((256x4)+1)x0.2 = 205 s. After all the measurements are taken the microcontroller automatically calculates and switches the network to the optimum capacitance, hence the plus one cycle needed on the full sweep time.

Table 7.4: Results for the Pulse-Echo using hardware peak detector for both transducers. It can be observed that the cases in which the unmatched transducer's impedance value is more distant from the source's also necessitate a higher capacitance to match, and the matching provides a higher gain. The HWS2225 transducer, at lower frequencies, benefits the most from the one-parallel-element matching network.

	RPDR#2's EMAT				HWS2225			
	Optimun Capacitance Found [nF]	No network pk-pk [V]	Optimal network pk-pk [V]	Gain [db]	Optimun Capacitance Found [nF]	No network pk-pk [V]	Optimal network pk-pk [V]	Gain [db]
2 MHz Aut.	2.45	402.9	897.15	6.9533	2.795	360.75	981.75	8.6958
3 MHz Aut.	1	352.65	621.15	4.9170	1.235	289.5	694.8	7.6042
4 MHz Aut.	0.5	356.7	403.35	1.0675	0.61	276	459	4.4180

8 Conclusion

Electromagnetic acoustic transducers are essential devices in several ultrasonic applications, but intrinsically they have low efficiency. Therefore, it is vital to use an impedance matching network in order to increase its signal-to-noise ratio. This process of impedance matching can be time-consuming and depends on various factors, such as the transducers, the excitation frequency, and the lift-off, among others. Many of these factors often change during laboratory testing or field applications. Therefore, automation of the impedance matching process can be of great benefit to the use of EMATs.

In this thesis, a simplified one-element impedance matching network was proposed, evaluated, and compared to the traditional full L-matching network. The one-element network's optimal values were theoretically derived, and numerical simulations were carried out in order to confirm their performance compared to a non-optimal one-element network, with the same values as the full L-network. The possibility of using one-element networks to calculate EMAT impedance is also proposed. Two models of spiral-coil EMAT were evaluated and their full bandwidth was determined for each of the matching networks. Depending on the intended excitation frequency, the one-element networks can provide a large part of the performance of the full L-network. The one-element networks also work better in a wide range of frequencies because it is not necessary to change their layout or the type of component, only the component's value. The one-element networks require only capacitors, which has some advantages compared to inductors.

Automatic and manual networks were designed and physically built. Experimental setups were devised and performed. The resulting experimental curves of voltage across the EMAT as a function of the network's capacitance were compared to the theoretical ones. The automatic matching process proved to be more than twice as fast as the manual one, providing similar matching results. Compared to the non-matched setup, the automatic impedance matching network provided from 2.6 to 5.6 dB gain in the RPDR's EMAT voltage signal. For this transducer, the matching network provided a higher improvement at lower frequencies. The HWS2225 is naturally more efficient, therefore the improvement provided by the matching network only spanned from 3.0 to 3.9 dB. The main advantage of the automatic network is the confidence that the best configuration for each setup can be used.

8.1 Future Work

Future work will aim to build an automatic full L-network so that it can be experimentally compared to both one-element networks simply by setting one of the equivalent values to zero. This network should also minimize its spurious effects, to achieve better results. It is also important to integrate ease-of-use elements, the peak detector explored here being the first example, but there are many more that can be incorporated. Reducing the setup time of the matching network is vital when considering the practicality compared to manual matching networks. Another avenue that should be explored is better search algorithms. The bisection search method would be easy to implement for the theoretical values. However, with the noise observed in the experimental results, some adaptations would need to be made. The golden search method could be more appropriate. Still, there are ways to make the search more efficient, taking fewer measurements than the full sweep. This full L-network would be experimentally evaluated as a method to measure EMAT impedance, as mentioned in Section 3.4.2.

As a final plan, it would be possible to make a more comprehensive network that incorporates both L-network layouts, and both types of elements in a wide range of values. To determine the values needed, an extensive study of the different factors that affect impedance matching is warranted. It can include, for example, the impedance analysis of many transducers in a wide range of conditions. This network would be capable of matching any EMAT, under any condition.

Bibliography

[1] L. W. Schmerr, "Fundamentals of ultrasonic nondestructive evaluation: A modeling approach." Springer, 2016.

[2] A. C. Kubrusly and S. Dixon, "Application of the reciprocity principle to evaluation of mode-converted scattered shear horizontal (SH) wavefields in tapered thinning plates," *Ultrasonics*, vol. 117, p. 106544, 2021.

[3] M. Hirao and O. H, *EMATs for Science and Industry: Noncontacting Ultrasonic Measurements.* Springer, 2017.

[4] J. L. Rose, *Ultrasonic Guided Waves in Solid Media.* Cambridge University Press, 2014.

[5] J. N. D. Cheeke, *Fundamentals and Applications of Ultrasonic Waves, 2nd edition.* CRC Press, 2017.

[6] M. Chen, Q. Huan, and F. Li, "A unidirectional SH wave transducer based on phase-controlled antiparallel thickness-shear (d15) piezoelectric strips," *Theoretical and Applied Mechanics Letters*, vol. 10, no. 5, pp. 299–306, 2020.

[7] H. Miao, Q. Huan, F. Li, and G. Kang, "A variable-frequency bidirectional shear horizontal (SH) wave transducer based on dual face-shear (d24) piezoelectric wafers," *Ultrasonics*, vol. 89, pp. 13–21, 2018.

[8] "Shear horizontal wave transducers for structural health monitoring and nondestructive testing: A review," *Ultrasonics*, vol. 114, p. 106355, 2021.

[9] J. L. Rose, D. Jiao, and J. Spanner, *Ultrasonics Guided Waves for Piping Inspection.* Boston, MA: Springer US, 1997, pp. 1285–1290.

[10] Z. W. B. Maxfield, "Electromagnetic acoustic transducers for nondestructive evaluation," *ASM Handbook, Volume 17, Nondestructive Evaluation of Materials Aquil Ahmad and Leonard J. Bond, editors.*

[11] Y. Wu and Y. Wu, "The effect of magnet-to-coil distance on the performance characteristics of emats," *Sensors*, vol. 20, 2020.

[12] X. S. Y. S. L. Wang, J.; Wu, “Study of the influence of the backplate position on emat thickness-measurement signals,” 2022.

[13] L. H. X. Ding, X. Wu, “Lift-off performance of receiving emat transducer enhanced by voltage resonance,” *18th World Conference on Nondestructive Testing*, 2018.

[14] Y. Zao, Q. Ouyang, X. Zhang, S. Hou, and M. Fang, “The dynamic impedance matching method for high temperature electromagnetic acoustic transducer,” in *2017 29th Chinese Control And Decision Conference (CCDC)*, 2017, pp. 1923–1927.

[15] S. Wenze, W. Chen, C. Lu, J. Zhang, Y. Chen, and W. Xu, “Optimal design of spiral coil emats for improving their pulse compression effect,” *Journal of Nondestructive Evaluation*, vol. 40, 06 2021.

[16] C. Kong, “A general maximum power transfer theorem,” *IEEE Transactions on Education*, vol. 38, no. 3, pp. 296–298, 1995.

[17] Y. Kuang, Y. Jin, S. Cochran, and Z. Huang, “Resonance tracking and vibration stablilization for high power ultrasonic transducers,” *Ultrasonics*, vol. 54, pp. 187–194, 2014.

[18] D. M. Pozar, *Microwave Engineering, 4th edition, chapters 2.6 and 5.1.* University of Massashussets at Amhert, 2012.

[19] X. Jian, S. Dixon, R. Edwards, and J. Morrison, “Coupling mechanism of an EMAT,” *Ultrasonics*, vol. 44, pp. e653–e656, 2006.

[20] K. F. Graff, *Wave motion in elastic solids.* Courier Corporation, 2012.

[21] L. M. Martinho, “Enhancement of unidirectional generation of sh ultrasonic waves with side-shifted periodic permanent magnet electromagnetic acoustic transducers and multiple rows of magnets.” Master’s thesis, Department of Electrical Engineering, Pontifícia Universidade Católica do Rio de Janeiro, 2022.

[22] B. A. Auld and R. E. Green, “Acoustic fields and waves in solids: Two volumes,” *Physics Today*, vol. 27, no. 10, pp. 63–64, 1974. [Online]. Available: https://doi.org/10.1063/1.3128926

[23] P. Sekhar and V. Uwizeye, “2 - review of sensor and actuator mechanisms for biomems,” in *MEMS for Biomedical Applications*, S. Bhansali and A. Vasudev, Eds. Woodhead Publishing, 2012, pp. 46–77.

[24] W. A. Kuperman, “Underwater acoustics,” in *Encyclopedia of Physical Science and Technology (Third Edition)*, R. A. Meyers, Ed. Academic Press, 2003, pp. 317–338.

[25] H. Chuck, *Handbook of Nondestructive Evaluation, Second Edition.* McGraw Hill Professional, 2012.

[26] “Ieee standard on piezoelectricity,” *ANSI/IEEE Std 176-1987*, 1988.

[27] C. Desilets, J. Fraser, and G. Kino, “The design of efficient broad-band piezoelectric transducers,” *IEEE Transactions on Sonics and Ultrasonics*, vol. 25, no. 3, pp. 115–125, 1978.

[28] R. Ribichini, “Modelling of electromagnetic acoustic transducers,” Ph.D. dissertation, Imperial College London, 2011.

[29] A. Allam, A. Bhardwaj, K. Sabra, and A. Erturk, “Piezoelectric transducer design and impedance tuning for concurrent ultrasonic power and data transfer,” in *Active and Passive Smart Structures and Integrated Systems XVI*, ser. Society of Photo-Optical Instrumentation Engineers (SPIE) Conference Series, J.-H. Han, S. Shahab, and J. Yang, Eds., Apr. 2022.

[30] S. Siripongdee and W. Jaikla, “Electronically controllable grounded inductance simulators using single commercially available ic: Lt1228,” *AEU - International Journal of Electronics and Communications*, 2017.

[31] P. Pelletier, J.-M. Guichon, J.-L. Schanen, and D. Frey, “Optimization of a dc capacitor tank,” *IEEE Transactions on Industry Applications*, vol. 45, no. 2, pp. 880–886, 2009.

[32] G. Petersen, “L-matching the output of a ritec gated amplifier to an arbitrary load,” accessed: March 2023. [Online]. Available: https://www.ritecinc.com/pdfs/match3.pdf

[33] “LTspice,” accessed: June 2023. [Online]. Available: https://www.analog.com/en/design-center/design-tools-and-calculators/ltspice-simulator.html

[34] “LTspice genealogy - the heritage of simulation ubiquity,” accessed: June 2023. [Online]. Available: https://ltwiki.org/index.php?title=LTspice_Genealogy_-_The_Heritage_of_Simulation_Ubiquity

[35] “Metallized polypropylene film capacitors ECWH(A) series,” accessed: July 2023. [Online]. Available: https://industrial.panasonic.com/cdbs/www-data/pdf/RDI0000/ABD0000C187.pdf

[36] "Metaltex miniature relay," accessed: May 2023. [Online]. Available: https://www.metaltex.com.br/assets/produtos/pdf/ax.pdf

[37] "ESP32-WROVER-I ESP32-WROVER-IE Datasheet," accessed: January 2023. [Online]. Available: https://www.espressif.com/sites/default/files/documentation/esp32-wrover-e_esp32-wrover-ie_datasheet_en.pdf

[38] "Ultra-small, low-power, 12-bit analog-to-digital converter with internal reference," accessed: April 2023. [Online]. Available: https://cdn-shop.adafruit.com/datasheets/ads1015.pdf

[39] H. Kelley and G. Alonso, "LTC6244 high speed peak detector," accessed: May 2023. [Online]. Available: https://www.analog.com/en/technical-articles/ltc6244-high-speed-peak-detector.html

[40] J. Irazabal and S. Blozis, "APPLICATION NOTE AN10216-01 I2C MANUAL," 2003, accessed: July 2023. [Online]. Available: https://www.nxp.com/docs/en/application-note/AN10216.pdf